Isotropic Polyharmonic B-splines:
Scaling Functions and Wavelets

Dimitri Van De Ville *Member*, Thierry Blu *Member*, Michael Unser *Fellow*

Abstract

In this paper, we use polyharmonic B-splines to build multi-dimensional wavelet bases. These functions are non-separable, multi-dimensional basis functions that are localized versions of radial basis functions. We show that Rabut's elementary polyharmonic B-splines do not converge to a Gaussian as the order parameter increases, as opposed to their separable B-spline counterparts. Therefore, we introduce a more isotropic localization operator that guarantees this convergence, resulting into the isotropic polyharmonic B-splines. Next, we focus on the two-dimensional quincunx subsampling scheme. This configuration is of particular interest for image processing, because it yields a finer scale progression than the standard dyadic approach. However, up to now, the design of appropriate filters for the quincunx scheme has mainly been done using the McClellan transform. In our approach, we start from the scaling functions, which are the polyharmonic B-splines and as such explicitly known, and we derive a family of polyharmonic spline wavelets corresponding to different flavors of the semi-orthogonal wavelet transform; e.g., orthonormal, B-spline, dual. The filters are automatically specified by the scaling relations satisfied by these functions. We prove that the isotropic polyharmonic B-spline wavelet converges to a combination of four Gabor atoms, which are well separated in the frequency domain. We also show that these wavelets are nearly isotropic and that they behave as an iterated Laplacian operator at low frequencies. We describe an efficient FFT-based implementation of the discrete wavelet transform based on polyharmonic B-splines.

Index Terms

Polyharmonic B-splines, scaling functions, multiresolution analysis, isotropy, rotation invariance, quincunx lattice, wavelets, Gabor wavelets

D. Van De Ville , T. Blu , M. Unser are with the Biomedical Imaging Group (BIG), Swiss Federal Institute of Technology Lausanne (EPFL), Switzerland.

Isotropic Polyharmonic B-splines:
Scaling Functions and Wavelets

I. INTRODUCTION

Multiresolution analysis has proved to be a powerful framework for providing time-frequency localized expansions with applications in many areas of signal processing. The well-known one-dimensional algorithm for the discrete wavelet transform corresponds to a two-channel filterbank: it splits the signal into two subsampled channels (at the analysis side), and it offers perfect reconstruction after upsampling and filtering again at the synthesis side. The wavelet transform can also be formulated in the continuous time domain, an approach that is often favored by mathematicians [1], [2]. Instead of working directly with the filters, this representation considers continuously-defined basis functions; i.e., scaling functions and wavelets. Recently, it has been demonstrated that the scaling function can always be expressed as a convolution of a B-spline (its regular part) and a residual distribution without order nor smoothness [3].

In the context of image processing, the most frequently used two-dimensional wavelet transforms are separable; their basis functions and filters are simply tensor products of the one-dimensional ones. Unfortunately, these decompositions introduce preferred (vertical and horizontal) directions and create a "diagonal" cross-term that does not have a straightforward interpretation. This has motivated researchers to design better non-separable wavelet transforms. One option is to priviledge angular selectivity. Numerous directional wavelet transforms, both frames (i.e., redundant) and bases (i.e., non-redundant), have been proposed [4]–[11]. Such representations can serve to sparsely represent essential image features such as edges combined with their orientation. Another interesting option, which has received less attention, is to emphasize isotropy. A strong motivation for this kind of design is that many standard image processing algorithms exploit the rotation-invariant properties of filters such as the Gaussian and Laplacian.

Our construction starts from radial basis functions (RBF), which are isotropic versions of power functions. Rabut has introduced a scheme to produce basis functions that are localized versions of these RBFs—the so-called "elementary polyharmonic B-splines". These B-splines share many interesting properties with their classical 1D counterparts. While studying these functions we discovered that, contrary to our expectations, they fail to converge to a Gaussian as the order increases. Since it is very desirable to have Gaussian-like basis functions, which are isotropic and optimally localized in space-frequency in the sense specified by the uncertainty principle, we decided to further investigate this issue. This led us to the construction of the "isotropic polyharmonic B-splines", which is presented in Sect. II. Our scheme utilizes a more isotropic discretization of the Laplacian operator, which guarantees the desired Gaussian convergence property. The generalization remains valid in higher dimensions as well.

The isotropic polyharmonic B-spline is an interesting candidate to be used as a scaling function for a wavelet decomposition. First, it has been shown that any multi-dimensional scaling function of order γ can be represented as the convolution of a polyharmonic B-spline of order γ and a distribution with a bounded Fourier

transform [12], [13]. It is the polyharmonic B-spline that brings all the desirable mathematical properties. Second, the isotropic polyharmonic B-spline satisfies a wide variety of scaling relations; in fact, many more than the classical dyadic ones. Here, we will focus on a particularly interesting one in two dimensions: the quincunx subsampling scheme. This scheme provides a more progressive transition through scale than the dyadic subsampling scheme [14]–[19]. For each iteration, the number of samples is halved, so a single wavelet can be used to characterize each bandpass subband. Up to now, most research for quincunx subsampling has focused on filterbank design and it has been difficult to define general wavelet families, as in one dimension, due to the lack of multi-variate factorization theorems. One popular option to circumvent this difficulty is to use the McClellan transform that maps a one-dimensional design into a two-dimensional one [20]–[22].

In Sect. III, we consider an alternative approach and introduce new wavelet bases for the quincunx subsampling scheme based on the two-dimensional isotropic polyharmonic B-splines. Specifically, we present a semi-orthogonal design procedure that yields a complete family of polynomial isotropic polyharmonic B-spline wavelets. We demonstrate that these wavelets form Riesz bases and that they qualitatively behave as a γ-th order Laplacian operator for low frequencies, which is isotropic once more. We also prove that one particular wavelet—the isotropic polyharmonic B-spline wavelet—converges to the sum of four Gabor atoms as the order increases. Additionally, it behaves as (fractionally) iterated Laplacian (and therefore isotropic) operator for low frequencies. Clearly, in our design, the continuously-defined functions (scaling functions and wavelets) play a central role. Nevertheless, the associated filters, which are required to implement the transform, are automatically defined. Explicit formulas are given in the Fourier domain. The implementation of the discrete wavelet transforms is presented in Sect. IV.

II. POLYHARMONIC B-SPLINES

A. The univariate case: B-spline basis functions and signal spaces

The construction of the polyharmonic B-splines is best explained by using the analogy with the standard one-dimensional B-splines. In particular, we consider the symmetric B-spline of odd degree $2m - 1$, $m \in \mathbb{N} \backslash \{0\}$. Its Fourier transform is given by

$$\hat{\beta}^{2m-1}(\omega) = \left(\frac{4 \sin^2(\omega/2)}{\omega^2} \right)^m. \tag{1}$$

We recognize the localization filter as the numerator and the power function as the denominator. In the spatial domain, such a B-spline can be regarded as a localized version of the two-sided power function $|x|^{2m-1}$ [23]. Consequently, the B-splines are piecewise polynomials.

The B-splines span the integer-shift-invariant signal space

$$\mathcal{V}(\beta^{2m-1}) = \left\{ s(x) = \sum_k c(k)\beta^{2m-1}(x - k), c \in l_2(\mathbb{Z}) \right\}, \tag{2}$$

where $c(k)$ are coefficients that are used as weights for the shifted basis functions. The notation $\sum_k$ stands for the sum of all $k \in \mathbb{Z}$. An essential property [24] of each spline signal $s(x)$ of $\mathcal{V}(\beta^{2m-1})$ is that they satisfy

$$\frac{d^{2m}s(x)}{dx^{2m}} = 0, \quad \text{for } x \in \mathbb{R} \backslash \mathbb{Z}. \tag{3}$$

In fact, the two-sided power function $|x|^{2m-1}$ is the symmetric Green function (or fundamental solution) of the differential operator in (3); i.e., the solution of the differential operator that gives $\delta(x)$. This implies, among other things, that the signal space $\mathcal{V}(\beta^{2m-1})$ is also spanned by shifted versions of $|x|^{2m-1}$ [23]. Another important observation is that the localization filter of the B-spline, represented by the numerator of (1), is the most elementary discretization of the corresponding "ideal" differential operator (m-th iterate of a second derivative).

B. The polyharmonic case: from radial basis functions to B-splines

Historically, the first extension of the univariate spline principles to N dimensions—next to tensor products—consists of building splines $s(\mathbf{x})$, $\mathbf{x} \in \mathbb{R}^N$, that satisfy

$$\Delta^m s(\mathbf{x}) = 0, \quad \text{for } \mathbf{x} \in \mathbb{R}^N \backslash \mathbb{Z}^N, \tag{4}$$

where $\Delta = \sum_{i=1}^{N} \partial^2 / \partial x_i^2$ denotes the Laplacian operator. As in the one-dimensional case, such splines $s(\mathbf{x})$ can be represented as linear combinations of shifted Green functions of the m-iterated Laplacian, which are known to be

$$\rho(\mathbf{x}) = \|\mathbf{x}\|^{2m-N} \left(c_{N,m} \ln \|\mathbf{x}\| + c'_{N,m} \right) \quad \longleftrightarrow \quad \hat{\rho}(\boldsymbol{\omega}) = \frac{1}{\|\boldsymbol{\omega}\|^{2m}}, \tag{5}$$

where $c_{N,m}$ and $c'_{N,m}$ are some suitable constants ($c'_{N,\gamma}$ is zero when $2m - N$ is even, while $c_{N,\gamma}$ is zero otherwise). The functions $\rho(\mathbf{x})$ are better known as generalized thin plate splines, an interesting class of radial basis functions (RBF). Each spline in the space spanned by this type of RBFs can be written as

$$s(\mathbf{x}) = \sum_{\mathbf{k}} c(\mathbf{k}) \rho(\mathbf{x} - \mathbf{k}), \tag{6}$$

and will necessarily satisfy (4). Often a polynomial of degree $m - 1$ is added to the right-hand side of (6), however, on the (infinite) Cartesian grid $\mathbb{Z}^N$, this polynomial is automatically included in the closure of the span of the RBFs. These splines have been studied intensively for (finite) scattered data interpolation [25]–[31] and also for the representation of signals on a uniform grid [32]–[34]. Probably the earliest example has been given by Harder [25], which corresponds to $N = 2$ and $m = 2$.

The direct application of RBFs to interpolation, as in (6), poses various theoretical and practical difficulties. Therefore, it is interesting to look for better conditioned basis functions, such as B-splines, that span the same signal space but are essentially localized. Rabut [35] defined "elementary m-harmonic cardinal B-splines[1]" by choosing the localization filter as the most elementary discretization of the Laplacian.

Definition 1 (Elementary m-harmonic cardinal B-splines): Their definition in the Fourier domain is remarkably similar to the univariate case:

$$\hat{\phi}^m(\boldsymbol{\omega}) = \frac{\|2 \sin(\boldsymbol{\omega}/2)\|^{2m}}{\|\boldsymbol{\omega}\|^{2m}} = \left(\frac{4 \sum_{k=1}^{N} \sin^2(\omega_k/2)}{\sum_{k=1}^{N} \omega_k^2} \right)^m, \tag{7}$$

with $\sin(\boldsymbol{\omega}) = (\sin(\omega_1), \ldots, \sin(\omega_N))$. The parameter m is an integer with $m \geq N/2$.

---

[1]Rabut introduced this terminology: "elementary" to emphasize that they are obtained by using the most elementary discretization of the Laplacian operator; "m-harmonic" since they are in the span of the fundamental solution of $\Delta^m f = \delta$ (see also [32], [33]); "cardinal" due to the uniform grid; "B-splines" since they are "bell-shaped" and regularize the Dirac distribution.

Fig. 1. (a) Filter coefficients for Rabut's 2D discretization of the Laplacian operator ($m = 1$, $\gamma = 2$). (b) Filter coefficients for the isotropic 2D discretization of the Laplacian operator. (c) Filter coefficients for Rabut's 3D discretization of the Laplacian operator. (d) Filter coefficients for the isotropic 3D discretization of the Laplacian operator.

In Fig. 1 (a) and (c), we show the discretized Laplacian operator ($m = 1$) for the two-dimensional and three-dimensional case. From now on, we prefer to denote the polyharmonic B-splines by their order of approximation, which is given by $\gamma = 2m$ (see later). Therefore, we denote them also as $\phi^m = \phi_{2m} = \phi_\gamma$. The signal space generated by ϕ_γ, which is the same as that spanned by RBFs of degree $\gamma - N$, can be written as

$$\mathcal{V}(\phi_\gamma) = \left\{ \sum_{\mathbf{k}} c(\mathbf{k}) \phi_\gamma(\mathbf{x} - \mathbf{k}), c \in l_2(\mathbb{Z}^N) \right\}. \tag{8}$$

The polyharmonic B-splines defined in this way satisfy most of the properties of the conventional B-splines: close resemblance of their definition in the Fourier domain, convolution relation $\phi_{\gamma_1 + \gamma_2} = \phi_{\gamma_1} * \phi_{\gamma_2}$, partition of unity, total positivity ($\hat{\phi}_\gamma > 0$). These splines are also reported to be "bell-shaped" functions. Unfortunately, and despite the fact that they are generated by multiple convolutions, they do not converge toward a Gaussian as the order increases.

Proposition 1: The elementary m-harmonic cardinal B-splines violate the conditions for the applicability of the central limit theorem and do not converge towards a Gaussian as the order increases.

Proof: The central limit theorem guarantees the convergence of iterated convolutions to a Gaussian. However, it requires a well-defined second-order moment. The second-order moment can be identified in the Fourier domain by considering the Taylor series development of $\hat{\phi}_2(\boldsymbol{\omega})$ for $\boldsymbol{\omega} \to \mathbf{0}$:

$$\begin{aligned} \hat{\phi}_2(\boldsymbol{\omega}) &= \frac{4 \sum_{k=1}^{N} \sin^2(\omega_k/2)}{\sum_{k=1}^{N} \omega_k^2} \\ &= 1 - \frac{1}{12} \left(\frac{\sum_{k=1}^{N} \omega_k^4}{\sum_{k=1}^{N} \omega_k^2} \right) + \mathcal{O}(\|\boldsymbol{\omega}\|^4), \quad \boldsymbol{\omega} \to \mathbf{0}. \end{aligned} \tag{9}$$

The second term is not twice continuously differentiable at $\mathbf{0}$, which implies that the second-order moment does not exist[2]. Following the outline of the proof of the central limit theorem, we can find the limiting function,

[2]For the two-dimensional case, it is instructive to switch to polar coordinates, which amounts to replacing (ω_1, ω_2) by $(r_\omega \cos(\theta_\omega), r_\omega \sin(\theta_\omega))$ in Eq. (9).

using (9), as

$$
\begin{aligned}
\hat{\phi}_\gamma \left(\frac{\boldsymbol{\omega}}{\sqrt{\gamma}} \right) &\approx \left(1 - \frac{1}{\gamma} \frac{1}{12} \left(\frac{\sum_{k=1}^N \omega_k^4}{\sum_{k=1}^N \omega_k^2} \right) \right)^{\gamma/2} \\
&\longrightarrow \exp \left(-\frac{1}{24} \frac{\sum_{k=1}^N \omega_k^4}{\sum_{k=1}^N \omega_k^2} \right), \qquad \text{as } \gamma \to \infty,
\end{aligned}
$$

which, clearly, is not a Gaussian. ∎

Rabut [36] also defined "n-th level m-harmonic cardinal B-splines" that were primarily designed to be improved quasi-interpolants; i.e., functions that interpolate polynomials of higher degree than the elementary versions. The higher level polyharmonic splines only converge towards a degenerated Gaussian, namely a Dirac distribution.

C. Isotropic polyharmonic B-splines

The discretization of the Laplacian operator corresponding to the numerator of Eq. (7) uses the least possible number of filter coefficients. The downside of this approach is the non-convergence to a Gaussian, which can be explained by a lack of isotropy of the discrete approximation of the Laplacian. This motivates us to introduce the "isotropic polyharmonic B-splines" using a slightly different, but more isotropic, discretization of the Laplacian operator. Strictly speaking, these B-splines are only quasi-isotropic, but they do become more and more isotropic as the order increases. Notationally, we usually specify a filter $h(\mathbf{k})$, $\mathbf{k} \in \mathbb{Z}^N$, by its $\mathcal{Z}$-transform as

$$
H(\mathbf{z}) = \sum_{\mathbf{k}} h(\mathbf{k}) \mathbf{z}^{\mathbf{k}},
$$

where $\mathbf{z}^{\mathbf{k}}$ is a shortcut notation for $\prod_{i=1}^N z_i^{k_i}$. We obtain its frequency response by putting $\mathbf{z} = e^{j\boldsymbol{\omega}}$, i.e., $H(e^{j\boldsymbol{\omega}})$.

Definition 2 (Isotropic polyharmonic B-splines): For $N = 2$ and 3, the isotropic polyharmonic B-splines of order γ are defined in the Fourier domain as

$$
\hat{\beta}_\gamma(\boldsymbol{\omega}) = \frac{V_\gamma(e^{j\boldsymbol{\omega}})}{\|\boldsymbol{\omega}\|^\gamma} \tag{10}
$$

where $V_\gamma(e^{j\boldsymbol{\omega}}) = V_2(e^{j\boldsymbol{\omega}})^{\gamma/2}$ and

$$
V_2(e^{j\boldsymbol{\omega}}) = 4 \sum_{k=1}^N \sin^2 \left(\frac{\omega_k}{2} \right) - \frac{8}{3} \sum_{k=1}^{N-1} \sum_{l=k+1}^N \sin^2 \left(\frac{\omega_k}{2} \right) \sin^2 \left(\frac{\omega_l}{2} \right). \tag{11}
$$

The second term in $V_2(e^{j\boldsymbol{\omega}})$ is a slight change of the elementary localization operator, but is essential to ensure the Gaussian convergence. Moreover, using standard trigonometric formulæ, one checks that $V_2(e^{j\boldsymbol{\omega}})$ is positive for $N = 2, 3$, because it can be expressed as a sum of positive quantities:

$$
V_2(e^{j\boldsymbol{\omega}}) = \frac{4}{3}(4 - N) \sum_{k=1}^N \sin^2 \left(\frac{\omega_k}{2} \right) + \frac{2}{3} \sum_{k=1}^{N-1} \sum_{l=k+1}^N \left(\sin^2 \left(\frac{\omega_k + \omega_l}{2} \right) + \sin^2 \left(\frac{\omega_k - \omega_l}{2} \right) \right).
$$

For $N \geq 4$, it would be necessary to include higher order terms for the localization filter to be strictly positive— when $N = 4$, the present filter vanishes at $\omega = (\pi, \pi, \pi, \pi)$ which makes the lower Riesz bound ill-defined (see Section II-D.2).

Proposition 2: The isotropic polyharmonic B-splines converge to a Gaussian as the order γ increases.

Proof: Reconsider the development of the elementary polyharmonic B-splines of (9). Clearly, for the second

term to be isotropic, its numerator should be proportional to $(\sum_{k=1}^{N} \omega_k^2)^2$. This can be obtained by adding the missing crossterms to $\sum_{k=1}^{N} \omega_k^4$. It can be verified that the new numerator proposed in (10) results into

$$\hat{\beta}_\gamma \left(\frac{\boldsymbol{\omega}}{\sqrt{\gamma}} \right) = 1 - \frac{1}{24} \|\boldsymbol{\omega}\|^2 + \mathcal{O}(\|\boldsymbol{\omega}\|^4), \quad \text{as } \boldsymbol{\omega} \to \mathbf{0}. \tag{12}$$

The second-order moment is now a constant ($\gamma/12$), irrespective of the direction. This property ensures that the isotropic polyharmonic B-splines rapidly converge to a Gaussian as the order γ increases. ∎

We want to show the effect of the isotropic discretization of the Laplacian (i.e., for $\gamma = 2$), as compared to the elementary discretization. In the two-dimensional case, the adjustment term of the localization filter introduces new knots at the corners of the 3×3, see Fig. 1 (b). Interestingly, the proposed isotropic discretisation of the Laplacian can also be seen[3] as the particular combination

$$V_2(\mathbf{z}) = \frac{2}{3} L^+(\mathbf{z}) + \frac{1}{3} L^\times(\mathbf{z}),$$

where L^+ represents the elementary discretisation along the axes (i.e., the numerator of (7) for $m = 1$)

$$L^+(\mathbf{z}) = z_1 + z_1^{-1} + z_2 + z_2^{-1} - 4,$$

and $L^\times$ the elementary discretisation along the diagonals

$$L^\times(\mathbf{z}) = \frac{1}{2} \left(z_1 z_2 + z_1^{-1} z_2 + z_1 z_2^{-1} + z_1^{-1} z_2^{-1} - 4 \right).$$

For the three-dimensional case, we notice that not all coefficients of the $3 \times 3 \times 3$ cube are required, see Fig. 1 (d).

From now on, we consider the definition of the isotropic polyharmonic B-splines for any fractional order $\gamma \in \mathbb{R}$ with $\gamma > N/2$, since this extension does not present any theoretical difficulty, as long as we work in the Fourier domain. In Fig. 2, we show the 2D elementary and isotropic polyharmonic B-spline for $\gamma = 5$, respectively. These functions are easy to evaluate numerically, for any order γ, by resampling (10) with a sufficient number of points and applying an inverse FFT.

D. Key properties

We now present the key properties of the polyharmonic B-splines (both the elementary and the isotropic ones). When necessary, we make a distinction between both.

1) Partition of unity: The partition of unity property guarantees that the polyharmonic B-splines reproduce the constant:

$$\sum_{\mathbf{n} \in \mathbb{Z}^N} \beta_\gamma(\mathbf{x} - \mathbf{n}) = 1 \quad \longleftrightarrow \quad \hat{\beta}_\gamma(2\langle \mathbf{k}, \boldsymbol{\pi} \rangle) = \delta_{\mathbf{k}}, \quad \mathbf{k} \in \mathbb{Z}^N, \tag{13}$$

where we denote $\boldsymbol{\pi} = (\pi, \ldots, \pi)$. This can be established directly by checking that the condition on the righthand side is verified.

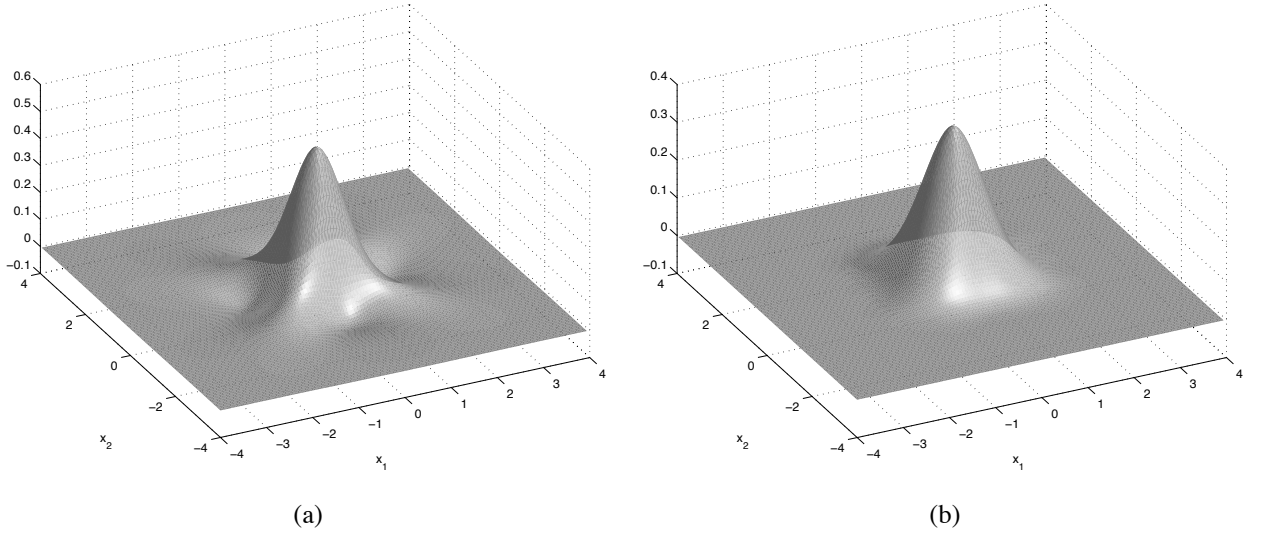---

[3]We thank an anonymous reviewer for this remark.

Fig. 2. Two-dimensional example of polyharmonic B-splines of fifth order ($N = 2$, $\gamma = 5$). (a) The elementary polyharmonic B-spline. (b) The isotropic polyharmonic B-spline.

2) Riesz basis: The polyharmonic B-splines $\{\beta_\gamma(\mathbf{x} - \mathbf{k})\}_{\mathbf{k} \in \mathbb{Z}^N}$ generate a Riesz basis; i.e., there exist two constants $0 < C_0, C_1 < \infty$ such that

$$C_0 \left\| c \right\|_{\ell_2} \le \left\| \sum_{\mathbf{n}} c_{\mathbf{n}} \beta_\gamma(\mathbf{x} - \mathbf{n}) \right\|_{L_2} \le C_1 \left\| c \right\|_{\ell_2}. \tag{14}$$

This condition is equivalent to

$$C_0 \le A_\gamma(e^{j\boldsymbol{\omega}}) \le C_1, \tag{15}$$

where $A_\gamma(e^{j\boldsymbol{\omega}})$ is the Fourier transform of the autocorrelation sequence $\langle \beta_\gamma(\cdot), \beta_\gamma(\cdot - \mathbf{n}) \rangle$; i.e.,

$$A_\gamma(e^{j\boldsymbol{\omega}}) = \sum_{\mathbf{n}} \langle \beta_\gamma(\cdot), \beta_\gamma(\cdot - \mathbf{n}) \rangle \exp(-j\langle \boldsymbol{\omega}, \mathbf{n} \rangle) \tag{16}$$

$$= \sum_{\mathbf{k}} \left| \hat{\beta}_\gamma(\boldsymbol{\omega} + 2\pi\mathbf{k}) \right|^2. \tag{17}$$

Using the convolution property of the polyharmonic B-spline, we can rewrite the autocorrelation filter as

$$A_\gamma(e^{j\boldsymbol{\omega}}) = \sum_{\mathbf{k}} \hat{\beta}_{2\gamma}(\boldsymbol{\omega} + 2\pi\mathbf{k}). \tag{18}$$

Given that $A_\gamma(e^{j\boldsymbol{\omega}}) \ge |\hat{\beta}_\gamma(\omega)|^2$ and that the continuous function $|\hat{\beta}_\gamma(\omega)|^2$ does not vanish inside $[-\pi, \pi]^N$, the existence of a lowerbound is trivial. The existence of the upperbound is also garanteed by the uniform convergence of the sum (18) as shown in App. A. As a sidenote, we would like to point out that there is a surprising connection between this autocorrelation filter and the so-called Epstein Zeta function which finds applications in crystallography (see [37]), in number theory (see [38]) and in quantum field theory (see [39]).

3) Orthonormal and dual flavors: The polyharmonic B-splines β_γ can be orthonormalized such that

$$\left\langle \beta_\gamma^\perp(\mathbf{x}), \beta_\gamma^\perp(\mathbf{x} - \mathbf{n}) \right\rangle = \delta_{\mathbf{n}}, \quad \text{for } \mathbf{n} \in \mathbb{Z}^N. \tag{19}$$

The Fourier expression of $\beta_\gamma^\perp$ is given by

$$\hat{\beta}_\gamma^\perp(\boldsymbol{\omega}) = \frac{\hat{\beta}_\gamma(\boldsymbol{\omega})}{\sqrt{A_\gamma(e^{j\boldsymbol{\omega}})}}. \tag{20}$$

Analogously, one can define the dual polyharmonic B-spline as the unique function $\beta_\gamma^\circ \in \mathcal{V}(\beta_\gamma)$ that is biorthonormal to $\beta_\gamma(\mathbf{x})$. In the Fourier domain, this yields:

$$\hat{\beta}_\gamma^\circ(\boldsymbol{\omega}) = \frac{\hat{\beta}_\gamma(\boldsymbol{\omega})}{A_\gamma(e^{j\boldsymbol{\omega}})}. \tag{21}$$

The dual splines are important since they allow us to specify the orthogonal projection of an L^2-function $f(\mathbf{x})$ onto $\mathcal{V}(\beta_\gamma)$; that is, the function of $\mathcal{V}(\beta_\gamma)$ that approximates $f(\mathbf{x})$ "best". Specifically, the projection $\mathcal{P}f(\mathbf{x})$ can be written equivalently as

$$\begin{aligned}
\mathcal{P}f(\mathbf{x}) &= \sum_{\mathbf{n}} \langle f(\cdot), \beta_\gamma^\circ(\cdot - \mathbf{n}) \rangle \beta_\gamma(\mathbf{x} - \mathbf{n}) \\
&= \sum_{\mathbf{n}} \langle f(\cdot), \beta_\gamma^\perp(\cdot - \mathbf{n}) \rangle \beta_\gamma^\perp(\mathbf{x} - \mathbf{n}) \\
&= \sum_{\mathbf{n}} \langle f(\cdot), \beta_\gamma(\cdot - \mathbf{n}) \rangle \beta_\gamma^\circ(\mathbf{x} - \mathbf{n}).
\end{aligned}$$

4) Spatial decay: Unlike traditional B-splines (1D or the tensor product extension) of integer order, the polyharmonic B-splines ($N \geq 2$) are not compactly supported. Rabut has shown that the elementary polyharmonic B-splines decay like $O(1/\|\mathbf{x}\|^{N+2})$ as $\|\mathbf{x}\| \to \infty$. The proof in [35, Th. 2] is quite technical but can be extended. First, when γ is not an even integer, the spatial decay becomes $O(1/\|\mathbf{x}\|^{N+\min(2,\gamma)})$. Second, for the isotropic polyharmonic B-splines, the new discretization of the Laplacian operator improves the smoothness of $\hat{\beta}_\gamma(\boldsymbol{\omega})$ around $\boldsymbol{\omega} = 0$ by 2 orders, which, in turn, increases the spatial decay of $\beta_\gamma(\mathbf{x})$ by 2 orders, at least for γ sufficiently large. Therefore, we obtain a $O(1/\|\mathbf{x}\|^{N+\min(4,\gamma)})$ decay. This faster decay property is another indication that the isotropic basis functions should be better localized.

5) Asymptotic convergence: As a result of the central limit theorem and Proposition 2, we also know that the isotropic polyharmonic B-spline tend to the following isotropic Gaussian as γ increases:

$$\beta_\gamma(\mathbf{x}) \approx \left(\frac{6}{\pi\gamma}\right)^{N/2} \exp\left(-\frac{6\|\mathbf{x}\|^2}{\gamma}\right), \tag{22}$$

whose standard deviation is $\sigma = \sqrt{\gamma/12}$. The normalized squared difference between β_γ and its Gaussian limiting function is below 5% for $\gamma \geq 3$. For the case $\gamma = 5$ of Fig. 2 (b), the difference barely reaches 3%.

Consequently, the order provides a tuning parameter for the size of the support, allowing us to search for an optimal tradeoff between spatial and spectral selectivity. Due to the convergence to a Gaussian, the isotropic polyharmonic B-splines tend to be asymptotically optimally localized in the sense of the Heisenberg uncertainty principle. More precisely, the product of their spatial and spectral bandwidth, defined as

$$S_{\beta_\gamma} S_{\hat{\beta}_\gamma}, \quad \text{with } S_{\beta_\gamma} = \left(\frac{\int \|\boldsymbol{\tau}\|^2 |\beta_\gamma(\boldsymbol{\tau})|^2 \, d\boldsymbol{\tau}}{\int |\beta_\gamma(\boldsymbol{\tau})|^2 \, d\boldsymbol{\tau}}\right)^{1/2}. \tag{23}$$

reaches the minimum $1/2$ as γ increases.

6) Order of approximation: Similar to classical B-splines, polyharmonic B-splines can approximate a given (well-behaved) function $f(\mathbf{x})$ to any required accuracy by projecting it onto a rescaled spline space with step size h. This property is related to the rate of decrease when the sampling grid gets finer of the approximation error between $f(\mathbf{x})$, where $f(\mathbf{x})$ and its γ-th derivative are in L_2, and the best polyharmonic B-spline representation:

$$\inf_{c(\mathbf{n})} \left\| f(\mathbf{x}) - \sum_{\mathbf{n}} c(\mathbf{n})\beta_\gamma\left(\mathbf{x}/h - \mathbf{n}\right) \right\|_{L_2} \leq \text{Const} \times h^\gamma, \tag{24}$$

where the constant depends on f and γ, but not on h. Given their Fourier definition, it is easy to show that

$$\forall \mathbf{k} \in \mathbb{Z}^N\backslash\{0\}, \hat{\beta}_\gamma(2\pi\mathbf{k} + \boldsymbol{\omega}) = O(\|\boldsymbol{\omega}\|^\gamma), \quad \text{for } \boldsymbol{\omega} \to \mathbf{0}, \tag{25}$$

which implies that the order of approximation for polyharmonic B-splines corresponds to γ [40], [41], thus justifying our terminology and notation for the γ-th order polyharmonic B-spline β_γ.

III. MULTI-RESOLUTION ANALYSIS

In this section, we investigate the multiresolution properties of the polyharmonic B-splines. Madych [42], [43] showed already that certain polyharmonic splines are perfectly valid scaling functions. Micchelli et al. [44] constructed pre-wavelets from (elliptic) polyharmonic B-splines for dyadic subsampling schemes. Here we will start from the isotropic polyharmonic B-splines to build semi-orthogonal wavelet bases. First, we briefly show that isotropic polyharmonic B-splines are admissible scaling functions that satisfy a whole variety of scaling relations. We then concentrate on the 2D quincunx subsampling scheme. When necessary, we will emphasize instances where we encounter an important difference between the elementary polyharmonic B-splines and the isotropic ones.

A. Scaling function and scaling relations

We want to define a dilation matrix $\mathbf{M}$ that maps every point $\mathbf{k} \in \mathbb{Z}^N$ to a subset of $\mathbb{Z}^N$. Therefore, we introduce $\mathbf{M}$ as a matrix of size $N \times N$ that contains only integer elements and with $|\det\mathbf{M}| \geq 2$. Another, more technical, requirement is that all eigenvalues of $\mathbf{M}$ should be strictly greater than 1; i.e., $\mathbf{M}$ should be a dilation in all directions [45].

We now recall the approximation space spanned by the polyharmonic B-splines, $\mathcal{V}(\beta_\gamma)$, as defined in Eq. (8). Similarly, we consider the approximation space $\mathcal{V}_\mathbf{M}$ at a finer resolution $\mathbf{M}$ as

$$\mathcal{V}_\mathbf{M} = \text{span}_{\mathbf{n}\in\mathbb{Z}^N}\left\{\beta_\gamma(\mathbf{M}\mathbf{x} - \mathbf{n})\right\}, \tag{26}$$

where we will further elaborate on the admissible choices of $\mathbf{M}$ later on. The idea is to generate a sequence of embedded subspaces of $L_2(\mathbb{R}^2)$:

$$\cdots \mathcal{V}_{\mathbf{M}^{-1}} \subset \mathcal{V}_{\mathbf{M}^0} \subset \mathcal{V}_\mathbf{M} \subset \mathcal{V}_{\mathbf{M}^2} \subset \cdots L_2. \tag{27}$$

Mallat [1] defined the minimal requirements that a scaling function needs to satisfy to generate an MRA. These requirements are functionally equivalent to: (i) Riesz conditions to ensure that we have shift-invariant subspaces; (ii) Partition of unity to guarantee the convergence $\lim_{i\to\infty} \mathcal{V}_{\mathbf{M}^i} = L_2$; (iii) Scaling relation for $\mathbf{M}$. The first

two properties have already been proven in the previous section. The scaling relation brings along the space inclusion property; i.e., it expresses β_γ in the finer resolution space:

$$\beta_\gamma(\mathbf{x}) = \sum_\mathbf{n} b_\gamma(\mathbf{n}) \beta_\gamma(\mathbf{Mx} - \mathbf{n}), \tag{28}$$

or, equivalently, in the Fourier domain:

$$B_\gamma(e^{j\boldsymbol{\omega}}) = |\det \mathbf{M}| \frac{\hat{\beta}_\gamma(\mathbf{M}^\mathrm{T}\boldsymbol{\omega})}{\hat{\beta}_\gamma(\boldsymbol{\omega})}. \tag{29}$$

In order to obtain a valid scaling filter $b(\mathbf{n})$, the respective denominators of $\hat{\beta}_\gamma(\mathbf{M}^\mathrm{T}\boldsymbol{\omega})$ and $\hat{\beta}_\gamma(\boldsymbol{\omega})$ in Eq. (29) need to cancel each other up to a scalar factor. Due to the isotropic denominator $\|\boldsymbol{\omega}\|^\gamma$ of the polyharmonic B-splines, $\mathbf{M}$ may correspond to any similarity transform; i.e., any rotation or symmetry combined with a dilation $|\det \mathbf{M}| \geq 2$. In particular, in two dimensions, the dilation matrix can be chosen

$$\mathbf{M} = \begin{bmatrix} a & b \\ -b & a \end{bmatrix}, \quad \text{or} \quad \mathbf{M} = \begin{bmatrix} a & b \\ b & -a \end{bmatrix}, \tag{30}$$

for a and b being integer and $a^2 + b^2 \geq 2$. It is interesting to mention that an MRA using the traditional tensor-product B-splines is much more restrictive; i.e., it requires the dilation matrix to be separable (corresponding to an integer scaling along each dimension).

Now we can define the wavelet space $\mathcal{W}_{\mathbf{M}^i}$ uniquely as the orthogonal complement of $\mathcal{V}_{\mathbf{M}^i}$ in $\mathcal{V}_{\mathbf{M}^{i+1}}$: $\mathcal{V}_{\mathbf{M}^i} \oplus \mathcal{W}_{\mathbf{M}^i} = \mathcal{V}_{\mathbf{M}^{i+1}}$. Finally, it is well-known that there exist $m = |\det \mathbf{M}| - 1$ wavelets $\psi_{(1)}, \ldots, \psi_{(m)}$, that span the residual spaces $\mathcal{W}_{\mathbf{M}^i}$:

$$\mathcal{W}_{\mathbf{M}^i} = \text{span}_{\mathbf{n} \in \mathbb{Z}^N} \left\{ \psi_{(1)}(\mathbf{M}^i \mathbf{x} - \mathbf{n}), \ldots, \psi_{(m)}(\mathbf{M}^i \mathbf{x} - \mathbf{n}) \right\}. \tag{31}$$

Many desirable mathematical properties of the wavelets, for instance the number of vanishing moments, are directly related to the order γ of the polyharmonic scaling function [12], [13].

B. Quincunx multi-resolution analysis

For the remaining part of this paper, we focus on the 2D quincunx dilation matrix, which is an interesting configuration for image processing (for which the traditional tensor product B-splines cannot be applied). As already mentioned in the introduction, the quincunx scheme provides a slower progression through scale than the traditional dyadic subsampling scheme. In addition, the wavelet space is spanned by only one wavelet, which simplifies its design and application.

The quincunx subsampling scheme, depicted in Fig. 3, can be represented by several possible dilation matrices [45]–[47]. For image processing, the most interesting one is based on a symmetry [17], [18], [48], [49] and is given by

$$\mathbf{D} = \begin{bmatrix} 1 & 1 \\ 1 & -1 \end{bmatrix}. \tag{32}$$

For an even number of iterations, the subsampled grid exactly coincides with the original cartesian grid at a twice coarser resolution; i.e., two subsequent scale reductions correspond to $\mathbf{D}^2 = 2\mathbf{I}$. As expected, the wavelet space is spanned by $|\det \mathbf{D}| - 1 = 1$ wavelet.
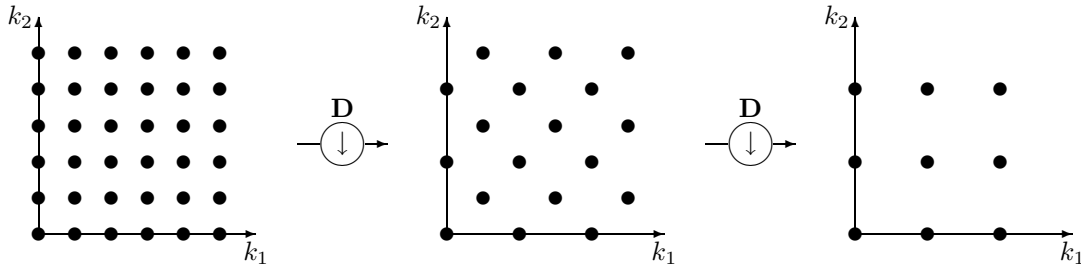
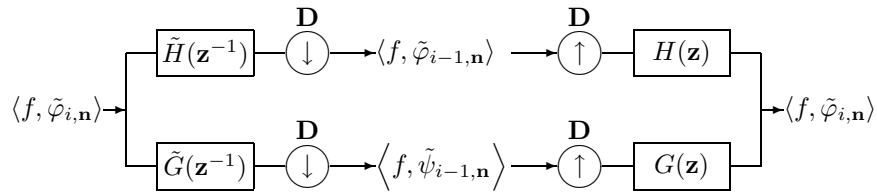Fig. 3. Quincunx subsampling scheme for two iterations.

Fig. 4. Analysis-synthesis filterbank for the 2D quincunx wavelet transform.

In Fig. 4, we show the wavelet transform algorithm for one iteration. We introduce the following notation: $\varphi_{i,\mathbf{n}}(\mathbf{x}) = \sqrt{2^i}\varphi(\mathbf{D}^i\mathbf{x} - \mathbf{n})$ and $\tilde{\varphi}_{i,\mathbf{n}}$ for the synthesis and analysis basis functions, respectively; $\psi_{i,\mathbf{n}}(\mathbf{x}) = \sqrt{2^i}\psi(\mathbf{D}^i\mathbf{x} - \mathbf{n})$ and $\tilde{\psi}_{i,\mathbf{n}}$ for the wavelets. The approximation of a function $f(\mathbf{x})$ at scale i can be written as

$$\sum_{\mathbf{n}} \langle f, \tilde{\varphi}_{i,\mathbf{n}}\rangle \varphi_{i,\mathbf{n}}(\mathbf{x}) = \sum_{\mathbf{n}} \langle f, \tilde{\varphi}_{i-1,\mathbf{n}}\rangle \varphi_{i-1,\mathbf{n}}(\mathbf{x}) + \sum_{\mathbf{n}} \langle f, \tilde{\psi}_{i-1,\mathbf{n}}\rangle \psi_{i-1,\mathbf{n}}(\mathbf{x}). \qquad (33)$$

For an efficient filterbank implementation, one directly works with the coefficients $c_{(i)}(\mathbf{n}) = \langle f, \tilde{\varphi}_{i,\mathbf{n}}\rangle$ and $d_{(i)}(\mathbf{n}) = \langle f, \tilde{\psi}_{i,\mathbf{n}}\rangle$ and computes the coefficients at the next coarser scale by filtering and downsampling. The scaling and wavelet filters are $\tilde{H}$ and $\tilde{G}$ on the analysis side, and H and G on the synthesis side, respectively. The conditions for perfect reconstruction that need to be satisfied by these filters are

$$\tilde{H}(\mathbf{z}^{-1})H(\mathbf{z}) + \tilde{G}(\mathbf{z}^{-1})G(\mathbf{z}) = 2, \qquad (34)$$

$$\tilde{H}(\mathbf{z}^{-1})H(-\mathbf{z}) + \tilde{G}(\mathbf{z}^{-1})G(-\mathbf{z}) = 0. \qquad (35)$$

C. Polynomial polyharmonic B-spline wavelets

In this section, we will follow the design procedure of [50], where the wavelet is selected orthogonal to all the integer-shifted versions of the scaling function. This leads to a wavelet transform that is usually refered to as "semi-orthogonal". A direct consequence of this strategy is that the wavelet spaces are orthogonal to each other: $\mathcal{W}_{\mathbf{M}^i} \perp \mathcal{W}_{\mathbf{M}^j}$, for $i \neq j$.

Since we will derive all our scaling functions and wavelets from the isotropic polyharmonic B-splines, we first show the scaling relation satisfied by these splines for the quincunx dilation matrix. By using Eq. (29)
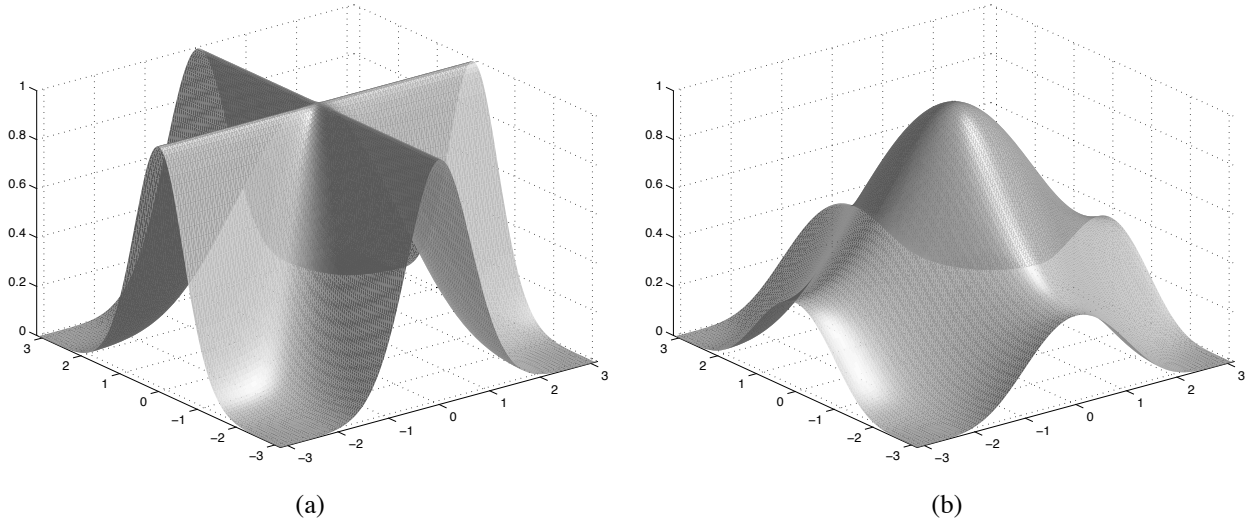
(a)

(b)

Fig. 5. The scaling filter $B_\gamma(e^{j\boldsymbol{\omega}})/2$ associated to the quincunx dilation matrix for $\gamma = 5$. (a) Elementary polyharmonic B-splines. (b) Isotropic polyharmonic B-splines.

with the quincunx dilation matrix (32), we obtain

$$B_\gamma(e^{j\boldsymbol{\omega}}) = 2^{1-\gamma/2} \left(\frac{\sin^2\left(\frac{\omega_1+\omega_2}{2}\right) + \sin^2\left(\frac{\omega_1-\omega_2}{2}\right) - \frac{2}{3}\sin^2\left(\frac{\omega_1+\omega_2}{2}\right)\sin^2\left(\frac{\omega_1-\omega_2}{2}\right)}{\sin^2\left(\frac{\omega_1}{2}\right) + \sin^2\left(\frac{\omega_2}{2}\right) - \frac{2}{3}\sin^2\left(\frac{\omega_1}{2}\right)\sin^2\left(\frac{\omega_2}{2}\right)} \right)^{\gamma/2}. \tag{36}$$

Figure 5 (b) shows the frequency response of this filter for order $\gamma = 5$. Also shown is the scaling filter for the elementary polyharmonic B-splines, which exhibits a much less favorable "cross-like" structure and this for any order γ. This is in contrast with the isotropic filter which becomes more and more Gaussian-like as γ increases.

1) Polyharmonic B-spline wavelet transform: As first example, we select the isotropic polyharmonic B-spline β_γ as scaling function φ. We look for the associated wavelet ψ, included in the function space $\mathcal{V}_{\mathbf{D}^0}$ at a finer scale,

$$\psi(\mathbf{D}^{-1}\mathbf{x}) = \sum_{\mathbf{n}} w(\mathbf{n})\beta_\gamma(\mathbf{x} - \mathbf{n}), \tag{37}$$

that also satisfies the orthogonality condition. Indeed, a necesary condition for $\mathcal{W}_{\mathbf{D}^{-1}} \perp \mathcal{V}_{\mathbf{D}^{-1}}$ is

$$\left\langle \psi(\mathbf{D}^{-1}\mathbf{x}), \beta_\gamma(\mathbf{D}^{-1}\mathbf{x} - \mathbf{n}) \right\rangle = 0.$$

This condition can be expressed equivalently in the z-domain as

$$W(\mathbf{z})B_\gamma(\mathbf{z})A_\gamma(\mathbf{z}) + W(-\mathbf{z})B_\gamma(-\mathbf{z})A_\gamma(-\mathbf{z}) = 0. \tag{38}$$

It can be shown that the general solution of this equation is

$$W(\mathbf{z}) = -z_1^{-1}Q(\mathbf{z}^{\mathbf{D}})B_\gamma(-\mathbf{z}^{-1})A_\gamma(-\mathbf{z}), \tag{39}$$

where $Q(\mathbf{z})$ is an arbitrary polynomial in $\mathbf{z}$. Here $\mathbf{z}^{\mathbf{D}}$ is a shortcut notation for $(z_1z_2, z_1z_2^{-1})$; the Fourier transform of $Q(\mathbf{z}^{\mathbf{D}})$ corresponds to $Q(e^{j\mathbf{D}^{\mathbf{T}}\boldsymbol{\omega}})$. The most obvious choice is $Q(\mathbf{z}) = 1$, which gives us

$$\hat{\psi}(\mathbf{D}^{\mathbf{T}}\boldsymbol{\omega}) = \frac{W(e^{j\boldsymbol{\omega}})}{2}\hat{\beta}_\gamma(\boldsymbol{\omega}), \tag{40}$$

with $W(e^{j\boldsymbol{\omega}}) = -e^{-j\omega_1}B_\gamma(e^{-j(\boldsymbol{\omega}+\boldsymbol{\pi})})A_\gamma(e^{j(\boldsymbol{\omega}+\boldsymbol{\pi})})$. This wavelet is referred to as the "isotropic polyharmonic B-spline wavelet".

Of course, the polynomial $Q(\mathbf{z})$ needs to satisfy certain properties to obtain suitable wavelets that form a Riesz basis. This is expressed by the following theorem, which is valid for any scaling function and the quincunx subsampling scheme.

Theorem 1: Let $\varphi(\mathbf{x})$ be a valid scaling function for the quincunx subsampling scheme. Specifically, it has a scaling filter $B_\gamma(e^{j\boldsymbol{\omega}})$ and it forms a Riesz basis; i.e., the autocorrelation filter $A_\gamma(e^{j\boldsymbol{\omega}})$ is bounded by two constants $0 < C_0 \leq A_\gamma(e^{j\boldsymbol{\omega}}) \leq C_1 < \infty$. Then, the wavelet given by

$$\hat{\psi}(\mathbf{D}^{\mathrm{T}}\boldsymbol{\omega}) = \frac{W(e^{j\boldsymbol{\omega}})}{2}\hat{\varphi}(\boldsymbol{\omega}), \tag{41}$$

with $W(e^{j\boldsymbol{\omega}}) = -e^{-j\omega_1}Q(e^{j\mathbf{D}^{\mathrm{T}}\boldsymbol{\omega}})B_\gamma(e^{j(\boldsymbol{\omega}+\boldsymbol{\pi})})A_\gamma(e^{j(\boldsymbol{\omega}+\boldsymbol{\pi})})$ forms a Riesz basis as well, as long as $\left|Q(e^{j\boldsymbol{\omega}})\right|^2$ is also bounded by two constants $0 < C_0' \leq \left|Q(e^{j\boldsymbol{\omega}})\right|^2 \leq C_1' < \infty$.

Proof: We compute the autocorrelation filter of the wavelet $\hat{\psi}(\boldsymbol{\omega})$:

$$\begin{aligned}
R(e^{j\boldsymbol{\omega}}) &= \sum_{\mathbf{k}}\left|\hat{\psi}(\boldsymbol{\omega}+2\pi\mathbf{k})\right|^2 \\
&= \frac{\left|W(e^{j\mathbf{D}^{-\mathrm{T}}\boldsymbol{\omega}})\right|^2}{4}A_\gamma(e^{j\mathbf{D}^{-\mathrm{T}}\boldsymbol{\omega}}) + \frac{\left|W(e^{j(\mathbf{D}^{-\mathrm{T}}\boldsymbol{\omega}+\boldsymbol{\pi})})\right|^2}{4}A_\gamma(e^{j(\mathbf{D}^{-\mathrm{T}}\boldsymbol{\omega}+\boldsymbol{\pi})}) \\
&= A_\gamma(e^{j\mathbf{D}^{-\mathrm{T}}\boldsymbol{\omega}})A_\gamma(e^{j(\mathbf{D}^{-\mathrm{T}}\boldsymbol{\omega}+\boldsymbol{\pi})})\left|Q(e^{j\boldsymbol{\omega}})\right|^2\left(\frac{\left|B_\gamma(e^{j\mathbf{D}^{-\mathrm{T}}\boldsymbol{\omega}})\right|^2}{4}A_\gamma(e^{j\mathbf{D}^{-\mathrm{T}}\boldsymbol{\omega}}) + \frac{\left|B_\gamma(e^{j(\mathbf{D}^{-\mathrm{T}}\boldsymbol{\omega}+\boldsymbol{\pi})})\right|^2}{4}A_\gamma(e^{j(\mathbf{D}^{-\mathrm{T}}\boldsymbol{\omega}+\boldsymbol{\pi})})\right) \\
&= A_\gamma(e^{j\mathbf{D}^{-\mathrm{T}}\boldsymbol{\omega}})A_\gamma(e^{j(\mathbf{D}^{-\mathrm{T}}\boldsymbol{\omega}+\boldsymbol{\pi})})A_\gamma(e^{j\boldsymbol{\omega}})\left|Q(e^{j\boldsymbol{\omega}})\right|^2 .
\end{aligned} \tag{42}$$

Consequently, the wavelet forms a Riesz basis if we have $0 < C_0' \leq \left|Q(e^{j\boldsymbol{\omega}})\right|^2 \leq C_1' < \infty$. ∎

The construction of the wavelet that leads to (40) describes the synthesis side of the wavelet transform. The complete transform, as indicated by Eq. (33), also requires the analysis scaling function and wavelet. To obtain the corresponding analysis funtions, we compute the dual scaling function that is given by

$$\hat{\tilde{\varphi}}(\boldsymbol{\omega}) = \hat{\beta}_\gamma^\circ(\boldsymbol{\omega}) = \frac{\hat{\beta}_\gamma(\boldsymbol{\omega})}{A_\gamma(e^{j\boldsymbol{\omega}})}, \tag{43}$$

and we automatically obtain the associated dual scaling filter

$$B_\gamma^\circ(e^{j\boldsymbol{\omega}}) = \frac{A_\gamma(e^{j\boldsymbol{\omega}})}{A_\gamma(e^{j\mathbf{D}^{\mathrm{T}}\boldsymbol{\omega}})}B_\gamma(e^{j\boldsymbol{\omega}}). \tag{44}$$

In a way similar to (42), we find the autocorrelation of the polyharmonic B-spline wavelet $R_\gamma(e^{j\boldsymbol{\omega}})$. Then, the dual wavelet can be concisely defined as

$$\hat{\tilde{\psi}}(\boldsymbol{\omega}) = \hat{\psi}^\circ(\boldsymbol{\omega}) = \frac{\hat{\psi}(\boldsymbol{\omega})}{R_\gamma(e^{j\boldsymbol{\omega}})}. \tag{45}$$

The corresponding dual wavelet relation,

$$\hat{\psi}^\circ(\mathbf{D}^{\mathrm{T}}\boldsymbol{\omega}) = \frac{W^\circ(e^{j\boldsymbol{\omega}})}{2}\hat{\beta}_\gamma^\circ(\boldsymbol{\omega}), \tag{46}$$

is obtained from (40) with $W^\circ(e^{j\boldsymbol{\omega}}) = -e^{-j\omega_1}\frac{B_\gamma^\circ(e^{-j(\boldsymbol{\omega}+\boldsymbol{\pi})})}{A_\gamma(e^{j(\boldsymbol{\omega}+\boldsymbol{\pi})})}$.

In practice, an efficient filterbank implementation will directly rely on the scaling and wavelet filters to process the coefficients. Table I lists all the filters and functions involved for the isotropic polyharmonic B-spline wavelet transform. Figure 7 depicts the respective scaling functions and wavelets in the spatial domain.

TABLE I

OVERVIEW OF ISOTROPIC POLYHARMONIC B-SPLINE WAVELET TRANSFORM

	analysis	synthesis
scaling function	$\beta_{\gamma}^{\circ}(\mathbf{x}) \longleftrightarrow \frac{\hat{\beta}_{\gamma}(\boldsymbol{\omega})}{A_{\gamma}(e^{j\boldsymbol{\omega}})}$	$\beta_{\gamma}(\mathbf{x})$
scaling filter	$\tilde{H}(\mathbf{z}) = B_{\gamma}^{\circ}(\mathbf{z}) = \frac{A_{\gamma}(\mathbf{z})}{A_{\gamma}(\mathbf{z}^{\mathbf{D}})} B_{\gamma}(\mathbf{z})$	$H(\mathbf{z}) = B_{\gamma}(\mathbf{z})$
wavelet function	$\psi^{\circ}(\mathbf{x}) \longleftrightarrow \hat{\psi}^{\circ}(\boldsymbol{\omega}) = \frac{\hat{\psi}(\boldsymbol{\omega})}{R_{\gamma}(e^{j\boldsymbol{\omega}})}$	$\psi(\mathbf{x}) \longleftrightarrow \hat{\psi}(\boldsymbol{\omega}) = \frac{W(e^{j\mathbf{D}^{-\mathrm{T}}\boldsymbol{\omega}})}{2} \hat{\beta}_{\gamma}(\boldsymbol{\omega})$
wavelet filter	$\tilde{G}(\mathbf{z}) = W^{\circ}(\mathbf{z}) = -z_1^{-1} \frac{B_{\gamma}^{\circ}(-\mathbf{z}^{-1})}{A_{\gamma}(-\mathbf{z})}$	$G(\mathbf{z}) = W(\mathbf{z}) = -z_1^{-1} B_{\gamma}(-\mathbf{z}^{-1}) A_{\gamma}(-\mathbf{z})$
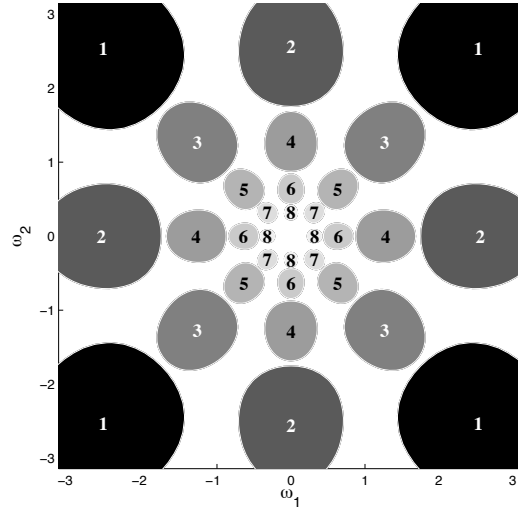
Fig. 6. Illustration of the tiling of the frequency domain for the polyharmonic B-spline wavelets of order $\gamma = 5$ up to the eight iteration. All contours shows their corresponding iteration number.

The *dual* isotropic polyharmonic B-spline wavelet transform can be found by interchanging the functions and filters between the analysis and synthesis part. Depending on the application, it might be desirable to put the B-spline either on the analysis or the synthesis side. The main feature of this wavelet decomposition is the excellent space-frequency localization of the B-spline scaling function and its wavelet. We already indicated that the isotropic polyharmonic B-splines tend to a Gaussian function as the order γ increases. Similarly, the associated wavelets tend to modulated Gaussians, also known as Gabor functions. In Appendix B, we give a proof of this convergence. In Fig. 6, we show the tiling of these wavelets in the frequency domain for eight consecutive iterations.

Indeed, Gabor wavelet-like decompositions have been found to be useful in many applications, as shown by the vast literature dealing with these functions [51]–[57]. Some examples include edge detection [58], [59], segmentation, texture analysis [60], modelling of primate's visual systems [61]–[63], statistical analysis of time-series (e.g., as in fMRI [64]), image analysis [65]–[67], hierarchical reconstruction [68], and so on. So the refinement filters of the isotropic polyharmonic B-spline wavelet transform might be good candidates to build a proper scale-space decomposition with a continuously-tunable order parameter.

2) Orthonormal polyharmonic B-spline wavelet transform: Another important wavelet transform is the orthonormal one, in which the scaling function and wavelets are orthonormal with regard to their own shifts. Note that for this transform, there will be no difference between the isotropic polyharmonic B-splines and the elementary ones: since both span the same space, their orthonormalized forms are equivalent. We note, however, that we have not yet seen these functions applied in the quincunx case, not to mention their fractional extensions.

The orthonormal polyharmonic B-spline is given by Eq.(20) and its corresponding scaling filter is

$$B_\gamma^\perp(e^{j\boldsymbol{\omega}}) = \sqrt{\frac{A_\gamma(e^{j\boldsymbol{\omega}})}{A_\gamma(e^{j\mathbf{D}^{\mathrm{T}}\boldsymbol{\omega}})}} B_\gamma(e^{j\boldsymbol{\omega}}). \tag{47}$$

Similarly, the orthonormal polyharmonic B-spline wavelet reads

$$\hat{\psi}^\perp(\boldsymbol{\omega}) = \frac{\hat{\psi}(\boldsymbol{\omega})}{\sqrt{R_\gamma(e^{j\boldsymbol{\omega}})}}, \tag{48}$$

with corresponding wavelet filter

$$W^\perp(e^{j\boldsymbol{\omega}}) = -e^{-j\omega_1} B_\gamma^\perp(e^{j(\boldsymbol{\omega}+\boldsymbol{\pi})}). \tag{49}$$

Some examples of such functions are shown in Fig. 7 (c)-(d).

In Appendix C, we prove the convergence of the orthonormal polyharmonic B-spline to the sinc function.

As for every linear orthonormal transform, the L_2-norm is conserved and white noise will remain white after transformation—a useful property for image denoising.

3) Generalized polyharmonic B-spline wavelet transforms: The B-spline, dual, and orthonormal flavor of the polyharmonic wavelet transforms are probably the most interesting candidates for applications. The design procedure for semi-orthogonal wavelet can also lead to other wavelets. In particular, the choice of $Q(\mathbf{z^D})$ in Eq. (39) is a degree of freedom that can be further explored. For example, we could select the interpolating polyharmonic B-spline at the synthesis side. This would eliminate the need of the initialization procedure that is needed to compute the initial values of the coefficients.

An interesting property of every polyharmonic wavelet is the behavior for low frequencies.

Proposition 3: The polyharmonic wavelets, obtained for any admissible choice of $Q(\mathbf{z^D})$, behave as the $\gamma/2$-th iterate of the Laplacian operator for low frequencies.

Proof: We consider Eqs. (39) and (40) for $\boldsymbol{\omega} \to \mathbf{0}$. The only term that tends to zero, and as such dominates the behavior of $\hat{\psi}(\boldsymbol{\omega})$ for $\boldsymbol{\omega} \to \mathbf{0}$, is $B_\gamma(e^{-j(\boldsymbol{\omega}+\boldsymbol{\pi})})$. Using (36), we can conclude that $\hat{\psi}(\boldsymbol{\omega}) \propto ||\boldsymbol{\omega}||^\gamma$ for low frequencies. ∎

This proposition shows how the operator that is related to the fundamental property of the polyharmonic B-splines gets transplanted to the wavelet functions.

In Fig. 8 (b), we show an example wavelet decomposition of the "zoneplate" image of (a). The subbands are organized in a way that is standard for the quincunx subsampling scheme; i.e., for odd iterations the odd lines are shifted by one pixel and then odd columns are subsampled (see also Sect. IV). The intensity values within each subband of Fig. 8 (b) have been rescaled to improve visualization. In the first subband, we only capture high frequency components at the corners of the frequency sweep. In fact, the local spatial frequency at these corners is close to the center frequency of the corresponding Gabor atoms depicted in Fig. 6. As we progress
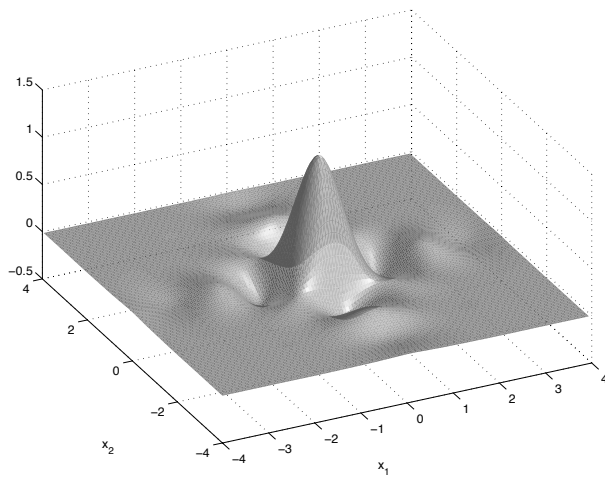
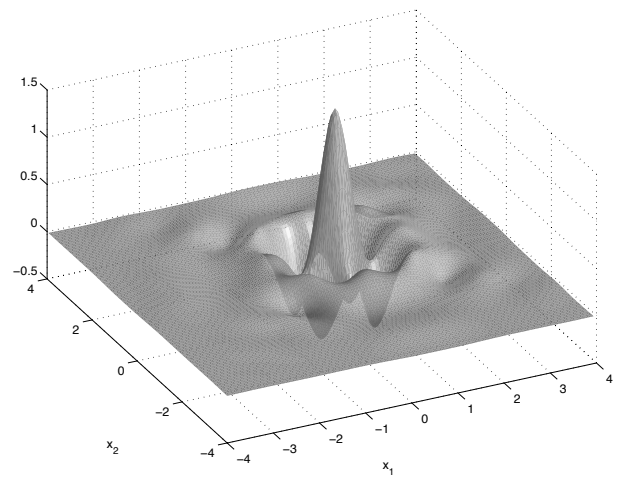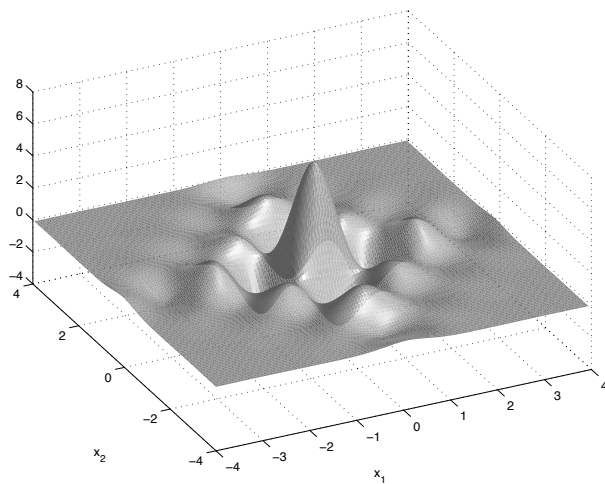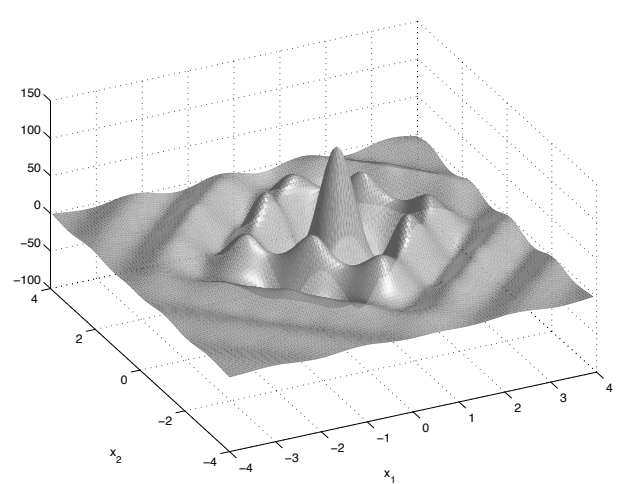B-spline flavor
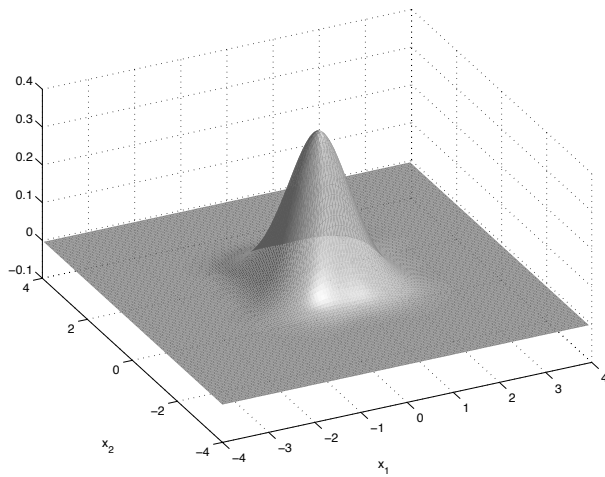
(a)
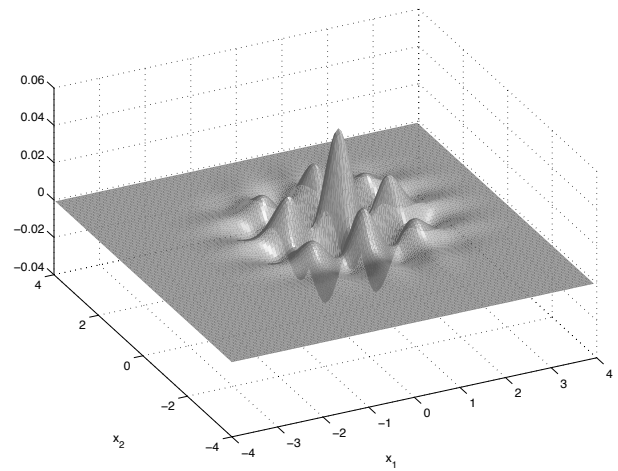
(b)

Orthonormal flavor

(c)

(d)

Dual flavor

(e)

(f)

Fig. 7. Various brands of scaling functions and wavelets based on isotropic polyharmonic B-splines of order $\gamma = 5.0$. (a) Isotropic polyharmonic B-spline. (b) Isotropic polyharmonic B-spline wavelet. (c) Orthonormalized polyharmonic B-spline. (d) Orthonormalized polyharmonic B-spline wavelet. (e) Dual isotropic polyharmonic B-spline. (f) Dual isotropic polyharmonic B-spline wavelet.

through scale, the "sensitive" regions detected by the wavelet have lower spatial frequencies. Interestingly, at some juncture, we switch from "Gabor regime" to "Laplacian regime".

IV. Implementation of the polyharmonic B-spline wavelet transform

All filters encountered in our construction are non-separable and infinitely supported. Therefore, a spatial implementation based on truncation turns out to be difficult and costly. However, the proposed polyharmonic wavelet transform can be advantageously implemented in the Fourier domain using FFTs, using the knowledge of the frequency response of the filters. Our Fourier-based implementation will also automatically take care of the boundaries by imposing periodic boundary conditions. Fourier-based implementations of the wavelet transform have been proposed before [22], [48], [49]. Using the same principle, we propose a slightly simplified version that is straightforward to implement and still performs very well.

To obtain the scaling and wavelet filters in the frequency domain, we need to compute the autocorrelation filter $A_\gamma(e^{j\boldsymbol{\omega}})$. This can be done in two dimensions by evaluating the sum of Eq. (18) for a sufficient number of terms. Another approach is to use a numerical algorithm in the spatial domain, for example see [69]. It is also possible to use a fastly converging method in the Fourier domain, as proposed in [70].

A. Fast Fourier-based discrete wavelet transform

The filterbank implementation of the wavelet transform directly deals with the coefficients $c_{(i)}(\mathbf{n})$ and $d_{(i)}(\mathbf{n})$, as defined before. However, all filters involved with the polyharmonic wavelet transform are infinitely supported. Because of this and also because our filters are characterized in the frequency domain, we propose the use of a Fourier-based implementation, ensuring perfect reconstruction for any choice of the order γ.

1) Initialization: At initialization, the signal is characterized by the coefficients $c_{(0)}(\mathbf{n}) = \langle f, \tilde{\varphi}_{0,\mathbf{n}} \rangle$, for a given support $S = \{\mathbf{n}|n_1, n_2 = 0, \dots, M-1\}$. Under the assumption that we only have access to the sample values $f(\mathbf{n})$, the data needs to be prefiltered such that the interpolating condition is satisfied; i.e.,

$$f(\mathbf{n}) = \sum_{\mathbf{m}} c_{(0)}(\mathbf{m})\beta_\gamma(\mathbf{n}-\mathbf{m}). \tag{50}$$

The proper interpolation prefilter is given by

$$P(e^{j\boldsymbol{\omega}}) = \left(\sum_{\mathbf{k}} \hat{\beta}_\gamma(\boldsymbol{\omega}+2\pi\mathbf{k})\right)^{-1}. \tag{51}$$

The same iterative numerical algorithm as used for the computation of the autocorrelation filter can be deployed to calculate this filter.

In practice, we first compute the Fourier coefficients of the data samples, for which we introduce the notation $F[\mathbf{k}] = F(e^{j2\pi\mathbf{k}/M}) = \sum_{\mathbf{n}\in S} f(\mathbf{n})e^{-j2\pi\langle\mathbf{n},\mathbf{k}\rangle/M}$, $\mathbf{k} \in S$. Note that the use of such a sampled Fourier representation corresponds to a periodic extension of the data in the spatial domain. The initial coefficients after prefiltering are

$$C_{(0)}[\mathbf{k}] = F[\mathbf{k}]P[\mathbf{k}]. \tag{52}$$
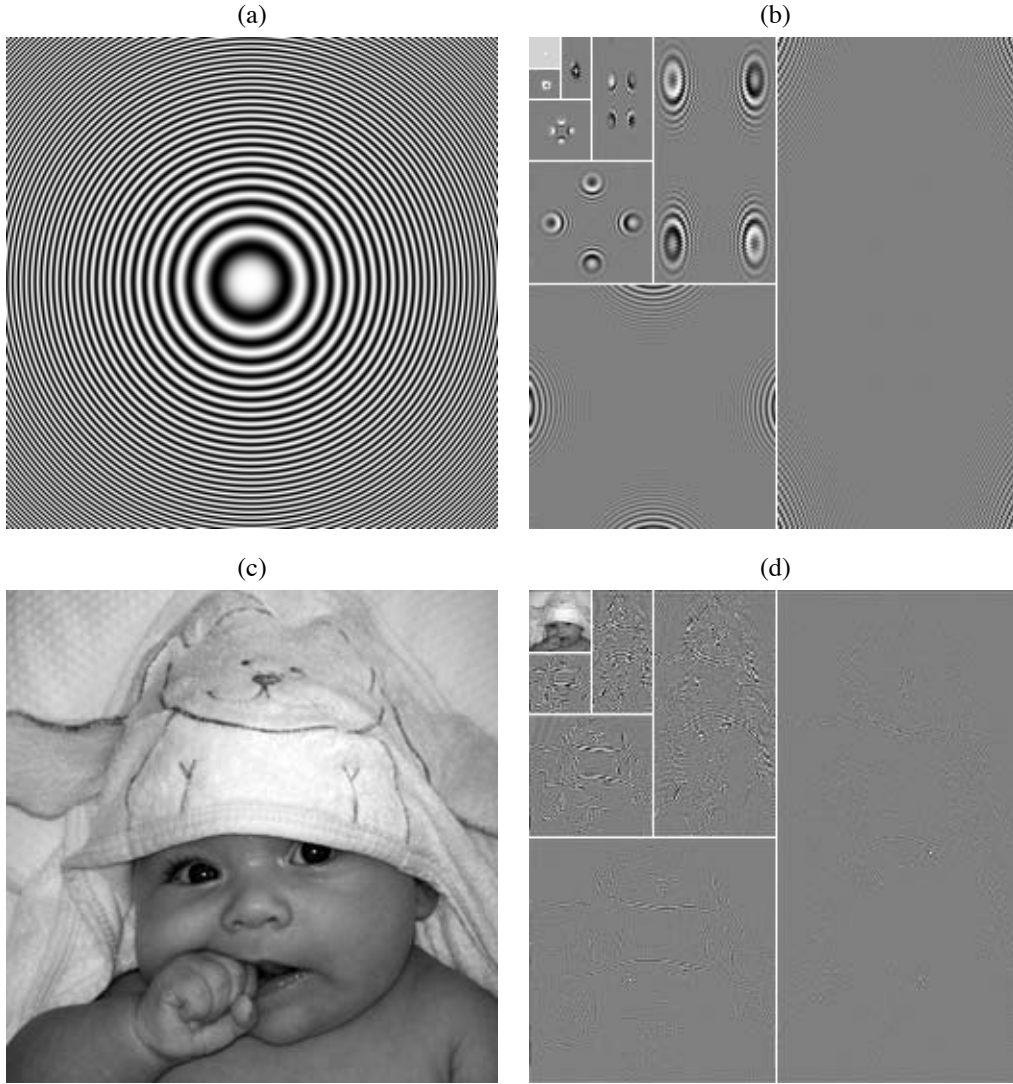
(a)

(b)

(c)

(d)

Fig. 8. (a) Test image "zoneplate". (b) Decomposition of "zoneplate" for 8 iterations and order $\gamma = 5$, B-splines at analysis. (c) Test image "Matteo". (d) Decomposition of "Matteo" after 6 iterations and order $\gamma = 5$, orthonormal flavor.

2) Analysis: An efficient implementation of the wavelet transform in the Fourier domain for the quincunx subsampling scheme can be obtained by pooling together two levels of the decomposition tree. Figure 9 shows a flowchart illustrating this approach. The indications $\mathcal{F}$ and $\mathcal{F}^{-1}$ mark where the data is respectively converted to and from the Fourier domain. The main steps of the algorithms are as follows.

1) The Fourier coefficients $C_{(0)}[\mathbf{k}]$ are filtered and then down- and upsampled, introducing redundancy in the Fourier domain. Taken together, such an operation results into

$$
\begin{aligned}
C_{(-1)}[\mathbf{k}'] &= \frac{1}{2}\left(\tilde{H}[\mathbf{k}']C_{(0)}[\mathbf{k}'] + \tilde{H}[\mathbf{k}' + (M/2, M/2)]C_{(0)}[\mathbf{k}' + (M/2, M/2)] \right), \\
D_{(-1)}[\mathbf{k}] &= \frac{1}{2}\left(\tilde{G}[\mathbf{k}]C_{(0)}[\mathbf{k}] + \tilde{G}[\mathbf{k} + (M/2, M/2)]C_{(0)}[\mathbf{k} + (M/2, M/2)] \right),
\end{aligned}
$$

where the index $\mathbf{k}'$ for the lowpass filter can be limited to $S' = \{\mathbf{n}|n_1 = 0, \ldots, M/2 - 1; n_2 = 0, \ldots, M - 1\}$. The easiest way to generate the highpass output $d_{(-1)}[\mathbf{k}']$ is by computing the inverse
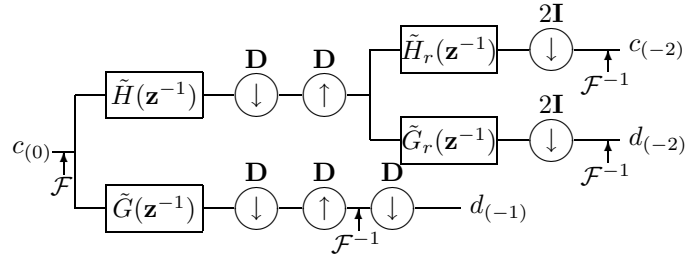
Fig. 9. Two levels of the quincunx wavelet decomposition stacked together. The symbols $\mathcal{F}$ and $\mathcal{F}^{-1}$ show where respectively the Fourier transform and the inverse Fourier transform is computed.

Fourier transform of $D_{(-1)}[\mathbf{k}]$ and performing the subsampling in the spatial domain.[4]

2) Next, the lowpass Fourier coefficients $C_{(-1)}[\mathbf{k}']$ are processed for the next iteration by the rotated filters, defined as $\tilde{H}_r[\mathbf{n}] = \tilde{H}[\mathbf{Dn} \mod (M, M)]$, $\tilde{G}_r[\mathbf{n}] = \tilde{G}[\mathbf{Dn} \mod (M, M)]$. So we get

$$C_{(-2)}[\mathbf{k}''] = \frac{1}{2}\left(\tilde{H}_r[\mathbf{k}'']C_{(-1)}[\mathbf{k}''] + \tilde{H}_r[\mathbf{k}'' + (0, M/2)]C_{(-1)}[\mathbf{k}'' + (0, M/2)]\right),$$

$$D_{(-2)}[\mathbf{k}''] = \frac{1}{2}\left(\tilde{G}_r[\mathbf{k}'']C_{(-1)}[\mathbf{k}''] + \tilde{G}_r[\mathbf{k}'' + (0, M/2)]C_{(-1)}[\mathbf{k}'' + (0, M/2)]\right),$$

where $\mathbf{k}'' \in S'' = \{\mathbf{n}|n_1, n_2 = 0, \ldots, M/2 - 1\}$. The outputs $c_{(-2)}[\mathbf{k}'']$ and $d_{(-2)}[\mathbf{k}'']$ are now directly obtained by applying the inverse Fourier transform to $C_{(-2)}[\mathbf{k}'']$ and $D_{(-2)}[\mathbf{k}'']$. Depending on the number of iterations, the remaining lowpass signal can be kept in the Fourier domain and further decomposed. A convenient way to arrange the coefficients is shown in Fig. 8 (b) and (d).

The filters $\tilde{H}$, $\tilde{G}$, and their rotated versions $\tilde{H}_r$, $\tilde{G}_r$ are precomputed at the size of the original data and subsampled after each other iteration. We also silently assumed that the analysis filters are reversed; i.e., their discrete Fourier transform corresponds to $\tilde{H}[\mathbf{k}] = \tilde{H}(e^{-j2\pi\mathbf{k}/M})$.

3) *Synthesis:* Using the same principles, one can obtain the synthesis algorithm as the flow graph transpose of the analysis algorithm. Again, all filters are precomputed.

B. Benchmark

The proposed algorithm can be translated seemlessly into a Matlab implementation. We compared the speed of our Fourier-based implementation in Matlab against the classical wavelet transform implementation which is available in the latest Matlab Wavelet Toolbox [71]. For this purpose, the image size is taken $M \times M$ where M varies from 128 to 1024 in steps of 16. This step size ensures a decomposition depth of 16 quincunx iterations or 8 separable iterations. In Fig. 10, we show timings obtained on an 2 GHz PowerPC processor (Apple G5). The fluctuations of the Fourier-based method are due to the specific implementation of the FFT [72] as used by Matlab. However, the general trend shows that the Fourier-based implementation appears to be competitive for image sizes up to about 512×512.

---

[4]It is also possible to exploit the redundancy of $D_{(-1)}[\mathbf{k}]$ in the Fourier domain, see [22].
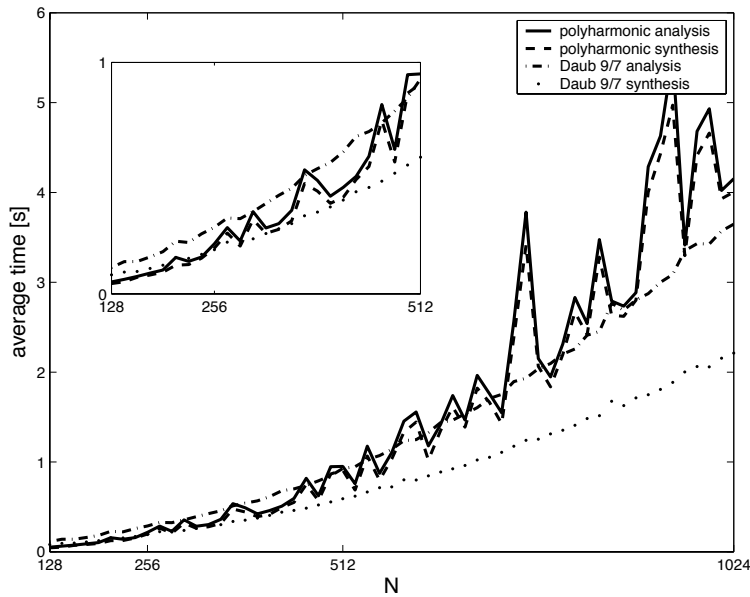
Fig. 10.   Execution times in seconds corresponding to the Fourier-based wavelet transform algorithm (blue lines) for the polyharmonic B-spline wavelet transform and Matlab's Wavelet Toolbox (red lines) for the Daubechies 9/7 (JPEG2000) wavelet transform. The size of the test image is $M \times M$ and varies from 128 to 1024 with a step of 16. The fluctuations of the Fourier-based algorithm are due to the specific implementation of the FFT algorithm.

Finally, we note that the current algorithm can be somewhat further improved at the cost of a slightly more complicated implementation. In particular, the analysis phase can be made as fast as the synthesis one by reducing the size of the high-pass inverse FFT at odd iterations [22].

V. Conclusion

In this paper, we have proposed to use isotropic polyharmonic B-splines to build a new family of wavelet bases. These B-splines are non-separable basis functions that are localized versions of generalized thin plate splines, and that converge towards a Gaussian as the order increases due to an improved localization operator that we have introduced. In the second part of the paper, we focused on the two-dimensional quincunx subsampling scheme to construct wavelet decompositions. Based on the function design in the continuous domain, we derived the suitable scaling and wavelet filters that we need for a fast discrete wavelet transform. Three flavors of semi-orthogonal designs were presented: orthonormal, B-spline, dual. The B-spline type wavelets converge to a sum of four Gabor atoms as the order increases. We also highlighted a fast implementation using FFTs.

Acknowledgments

Appendix A

Upper Riesz bound

We want to evaluate an upper bound over $\boldsymbol{\omega} \in \mathbb{R}^N$ for the the autocorrelation (18). First, we can restrict the values of $\boldsymbol{\omega}$ to $[-\pi, \pi]^N$ since the autocorrelation is 2π-periodic in every component ω_k of $\boldsymbol{\omega}$. Second, we easily check from (10) that $\hat{\beta}_\gamma(\boldsymbol{\omega}) \leq 1$ which means that $V_\gamma(e^{j\boldsymbol{\omega}}) \leq \|\boldsymbol{\omega}\|^\gamma \leq (\sqrt{N}\,\pi)^\gamma$.

Moreover, when $|\omega_k| \leq \pi$, the inequality $|\omega_k - 2\pi n_k| \geq \pi |n_k|$ is valid for all $n_k \in \mathbb{Z}$. This implies that

$$\|\boldsymbol{\omega} - 2\pi\mathbf{n}\| \geq \pi \|\mathbf{n}\| \tag{53}$$

and finally

$$
\begin{aligned}
A_\gamma(e^{j\boldsymbol{\omega}}) &= |\hat{\beta}_\gamma(\boldsymbol{\omega})|^2 + \sum_{\mathbf{n} \in \mathbb{Z}^N \setminus \{\mathbf{0}\}} \frac{V_{2\gamma}(e^{j\boldsymbol{\omega}})}{\|\boldsymbol{\omega} + 2\mathbf{n}\pi\|^{2\gamma}} \\
&\leq 1 + \sum_{\mathbf{n} \in \mathbb{Z}^N \setminus \{\mathbf{0}\}} \frac{(\sqrt{N}\,\pi)^{2\gamma}}{\|\boldsymbol{\omega} + 2\mathbf{n}\pi\|^{2\gamma}} \\
&\leq 1 + N^\gamma \sum_{\mathbf{n} \in \mathbb{Z}^N \setminus \{\mathbf{0}\}} \frac{1}{\|\mathbf{n}\|^{2\gamma}}
\end{aligned}
$$

which is known to be bounded whenever $2\gamma > N$. Note that this bound is not sharp as it tends to increase when γ increases. ∎

Appendix B

Convergence of the isotropic polyharmonic B-spline wavelet to Gabor wavelet

In this appendix, we derive the asymptotic form of the bidimensional (i.e., $N = 2$) isotropic polyharmonic B-spline wavelet. Before showing that it converges to the sum of four Gabor atoms, symmetrically placed in the frequency domain, we introduce the following lemma.

Lemma 1: For $\gamma \geq 3$, the autocorrelation filter $A_\gamma(e^{j\boldsymbol{\omega}})$ of the bidimensional isotropic polyharmonic B-spline is bounded over $\mathbb{R}^2$ as follows:

$$\sum_{\|\mathbf{n}\|^2 \leq 2} \left|\hat{\beta}_\gamma([\boldsymbol{\omega}] + 2\pi\mathbf{n})\right|^2 \leq A_\gamma(e^{j\boldsymbol{\omega}}) \leq (1+\epsilon) \sum_{\|\mathbf{n}\|^2 \leq 2} \left|\hat{\beta}_\gamma([\boldsymbol{\omega}] + 2\pi\mathbf{n})\right|^2, \tag{54}$$

where $\epsilon = 12\sqrt{3}\,(2/3)^\gamma$ tends to zero exponentially fast as $\gamma \to \infty$.

The notation $[\boldsymbol{\omega}]$ stands for the unique 2D vector in $[-\pi, \pi[^2$ such that $\boldsymbol{\omega} - [\boldsymbol{\omega}] = 2\mathbf{n}\pi$ for some 2D integer $\mathbf{n}$.

Proof: We first observe that we can restrict the range of values of $\boldsymbol{\omega}$ to $[-\pi, \pi]^2$ because the autocorrelation filter is 2π-periodic. Since the lower bound is trivial we concentrate on the upper bound. We use (53) over the autocorrelation sum restricted to $\|\mathbf{n}\|^2 \geq 3$, and find:

$$
\begin{aligned}
A_\gamma(e^{j\boldsymbol{\omega}}) &\leq \sum_{\|\mathbf{n}\|^2 \leq 2} \left|\hat{\beta}_\gamma(\boldsymbol{\omega} + 2\pi\mathbf{n})\right|^2 + \sum_{\|\mathbf{n}\|^2 \geq 3} \frac{V_{2\gamma}(e^{j\boldsymbol{\omega}})}{\|\pi\mathbf{n}\|^{2\gamma}} \\
&\leq \sum_{\|\mathbf{n}\|^2 \leq 2} \left|\hat{\beta}_\gamma(\boldsymbol{\omega} + 2\pi\mathbf{n})\right|^2 + \left|\hat{\beta}_\gamma(\boldsymbol{\omega})\right|^2 \sum_{\|\mathbf{n}\|^2 \geq 3} \frac{\|\boldsymbol{\omega}\|^{2\gamma}}{\|\pi\mathbf{n}\|^{2\gamma}} \\
&\leq \sum_{\|\mathbf{n}\|^2 \leq 2} \left|\hat{\beta}_\gamma(\boldsymbol{\omega} + 2\pi\mathbf{n})\right|^2 \left(1 + \sum_{\|\mathbf{n}\|^2 \geq 3} \frac{\|\boldsymbol{\omega}\|^{2\gamma}}{\|\pi\mathbf{n}\|^{2\gamma}}\right) \\
&\leq \sum_{\|\mathbf{n}\|^2 \leq 2} \left|\hat{\beta}_\gamma(\boldsymbol{\omega} + 2\pi\mathbf{n})\right|^2 \left(1 + \sum_{\|\mathbf{n}\|^2 \geq 3} \frac{2^\gamma}{\|\mathbf{n}\|^{2\gamma}}\right).
\end{aligned}
$$

We thus have to evaluate the quantity $2^\gamma \sum_{\|\mathbf{n}\|^2 \geq 3} \|\mathbf{n}\|^{-2\gamma}$. We denote by ν_N the number of (signed) integer solutions to the Diophantine equation: $n_1^2 + n_2^2 = N$. Obviously, $\nu_N \leq 2 \times 2\sqrt{N}$ because n_1 is necessarily in $[-\sqrt{N}, \sqrt{N}]$ and n_2 is uniquely determined by n_1 up to a sign. Then, we find:

$$
2^\gamma \sum_{\|\mathbf{n}\|^2 \geq 3} \|\mathbf{n}\|^{-2\gamma} = 2^\gamma \sum_{N \geq 3} \frac{\nu_N}{N^\gamma}
$$
$$
\leq 2^{\gamma+2} \sum_{N \geq 3} \frac{1}{N^{\gamma-1/2}},
$$

which is convergent because $\gamma - 1/2 > 1$. Now, it is well-known (see [73]) that the remainder of the Riemann zeta function is bounded according to $\sum_{N \geq N_0} N^{-s} \leq N_0^{-s+1}/(s-1)$. Applying this formula with $N_0 = 4$ and $s = \gamma - 1/2$, and taking into account that $\gamma \geq 3$, we find

$$
2^\gamma \sum_{\|\mathbf{n}\|^2 \geq 3} \|\mathbf{n}\|^{-2\gamma} \leq 2^{\gamma+2} \Big(\frac{1}{3^{\gamma-1/2}} + \frac{1}{(\gamma-3/2)3^{\gamma-3/2}} \Big) \leq 12\sqrt{3} \Big(\frac{2}{3} \Big)^\gamma
$$

which proves the lemma. ∎

Armed with this lemma, we can now proceed to the proof of our convergence theorem. The isotropic polyharmonic B-spline wavelet has been defined as

$$
2\hat{\psi}(\mathbf{D}^{\mathrm{T}}\boldsymbol{\omega}) = -e^{-j\omega_1} B_\gamma(e^{j(\boldsymbol{\omega}+\boldsymbol{\pi})}) A_\gamma(e^{j(\boldsymbol{\omega}+\boldsymbol{\pi})}) \hat{\beta}_\gamma(\boldsymbol{\omega}). \tag{55}
$$

Thanks to Lemma 1, the autocorrelation filter can be replaced by a finite sum when $\gamma \to \infty$; i.e.,

$$
2\hat{\psi}(\mathbf{D}^{\mathrm{T}}\boldsymbol{\omega}) = -e^{-j\omega_1} \sum_{\|\mathbf{n}\|^2 \leq 2} \Big(\underbrace{\hat{\beta}_2([\boldsymbol{\omega}+\boldsymbol{\pi}] + 2\pi\mathbf{n}) B_1(e^{j(\boldsymbol{\omega}+\boldsymbol{\pi})}) \hat{\beta}_1(\boldsymbol{\omega})}_{r_{\mathbf{n}}(\boldsymbol{\omega})} \Big)^\gamma \Big(1 + \mathcal{O}\big((2/3)^\gamma\big) \Big).
$$

By inspection, we observe that

$$
\sup_{\boldsymbol{\omega} \in \mathbb{R}^2} r_{\mathbf{n}}(\boldsymbol{\omega}) \approx \begin{cases} 0.05 & \text{for } \mathbf{n} = (-1,-1), (-1,1), (1,-1), (1,1) \\ 0.16 & \text{for } \mathbf{n} = (-1,0), (0,-1), (0,1), (1,0) \\ 0.4 & \text{for } \mathbf{n} = (0,0) \end{cases}
$$

which shows that, as $\gamma \to \infty$, $r_{\mathbf{0}}(\boldsymbol{\omega})^\gamma$ dominates the other $r_{\mathbf{n}}(\boldsymbol{\omega})^\gamma$ terms; i.e.,

$$
\hat{\psi}(\boldsymbol{\omega}) \approx -\frac{1}{2} e^{-j\frac{\omega_1+\omega_2}{2}} r_{\mathbf{0}}(\mathbf{D}^{-\mathrm{T}}\boldsymbol{\omega})^\gamma. \tag{56}
$$

As one can readily observe, $r_{\mathbf{0}}(\boldsymbol{\omega})$ has a fourfold symmetry: $r_{\mathbf{0}}(\omega_1, \omega_2) = r_{\mathbf{0}}(-\omega_1, \omega_2) = r_{\mathbf{0}}(\omega_1, -\omega_2) = r_{\mathbf{0}}(-\omega_1, -\omega_2)$. By inspection again, $r_{\mathbf{0}}(\boldsymbol{\omega})$ reaches its maximum $M \approx 0.4$ at $\boldsymbol{\omega} = (\omega', \omega')$ and at its other three symmetric positions $(-\omega', \omega'), (\omega', -\omega')$ and $(-\omega', -\omega')$, where $\omega' \approx 5.074$. This means that $\hat{\psi}(\boldsymbol{\omega})$ reaches its maximum at $\boldsymbol{\omega} = (\omega', 0), (-\omega', 0), (0, \omega')$ and $(0, -\omega')$.

In the neighborhood of $\boldsymbol{\omega}' = (\omega', 0)$ we consider the Taylor development

$$
\ln r_{(0,0)}(\mathbf{D}^{-\mathrm{T}}\boldsymbol{\omega}) = \ln M - \frac{1}{2} \Big(\frac{\omega_1 - \omega'}{s_1} \Big)^2 - \frac{1}{2} \Big(\frac{\omega_2}{s_2} \Big)^2 + \mathcal{O}(\|\boldsymbol{\omega} - \boldsymbol{\omega}'\|^3), \tag{57}
$$

with

$$
s_1 \approx 2.7, \quad s_2 \approx 2.36. \tag{58}
$$

Using the central limit theorem, we obtain

$$
\hat{\psi}(\boldsymbol{\omega}) \approx -\frac{M^\gamma}{2} e^{-j\frac{\omega_1+\omega_2}{2}} \big(\hat{g}(\omega_1, \omega_2) + \hat{g}(-\omega_1, \omega_2) + \hat{g}(\omega_2, \omega_1) + \hat{g}(\omega_2, -\omega_1) \big), \tag{59}
$$

with

$$\hat{g}(\boldsymbol{\omega}) = e^{-\frac{\gamma}{2}\left(\frac{\omega_1-\omega'}{s_1}\right)^2 - \frac{\gamma}{2}\left(\frac{\omega_2}{s_2}\right)^2} \quad \longleftrightarrow \quad \frac{s_1 s_2}{2\pi\gamma} e^{j\omega' x_1} e^{-\frac{s_1^2 x_1^2 + s_2^2 x_2^2}{2\gamma}}. \tag{60}$$

Finally, we state that the inverse Fourier transform of both sides is equivalent for large γ, providing

$$\psi(\mathbf{x}) \approx -\frac{M^\gamma s_1 s_2}{2\pi\gamma}\left(\cos\left(\omega' x_1 - \frac{\omega'}{2}\right) e^{-\frac{s_1^2(x_1-\frac{1}{2})^2 + s_2^2(x_2-\frac{1}{2})^2}{2\gamma}} + \cos\left(\omega' x_2 - \frac{\omega'}{2}\right) e^{-\frac{s_1^2(x_2-\frac{1}{2})^2 + s_2^2(x_1-\frac{1}{2})^2}{2\gamma}}\right). \tag{61}$$

Appendix C

Convergence of the orthonormal polyharmonic B-spline to the sinc function

We want to show that $\hat{\beta}_\gamma^\perp(\boldsymbol{\omega})$ tends to the function $\mathrm{rect}(\frac{\omega_1}{2\pi}) \cdot \mathrm{rect}(\frac{\omega_2}{2\pi})$ indicator of the square $[-\pi,\pi]^2$. Assume that $\boldsymbol{\omega}$ belongs to $[-\pi(1-\eta), \pi(1-\eta)]^2$ where η is some small positive quantity. Then according to the definition (20) and Lemma 1 we have

$$1 \geq |\hat{\beta}_\gamma^\perp(\boldsymbol{\omega})|^2 \geq \frac{|\hat{\beta}_\gamma(\boldsymbol{\omega})|^2}{\displaystyle\sum_{\|\mathbf{n}\|^2 \leq 2} \left|\hat{\beta}_\gamma(\boldsymbol{\omega} + 2\pi\mathbf{n})\right|^2} + \mathcal{O}(2/3)^\gamma$$

$$\geq \frac{1}{1 + \displaystyle\sum_{\|\mathbf{n}\|=1}^{\sqrt{2}} \frac{|\boldsymbol{\omega}|^{2\gamma}}{|\boldsymbol{\omega} + 2\pi\mathbf{n}|^{2\gamma}}} + \mathcal{O}(2/3)^\gamma.$$

Moreover, using the obvious inequality $|n_1| + |n_2| \leq \|\mathbf{n}\|^2$ and the hypothesis that $|\omega_k| \leq \pi(1-\eta)$, we find

$$\|\boldsymbol{\omega} + 2\mathbf{n}\pi\|^2 = \|\boldsymbol{\omega}\|^2 + 4\pi\mathbf{n}^T\boldsymbol{\omega} + 4\pi^2\|\mathbf{n}\|^2$$

$$\geq \|\boldsymbol{\omega}\|^2 - 4\pi^2(1-\eta)(|n_1| + |n_2|) + 4\pi^2\|\mathbf{n}\|^2$$

$$\geq \|\boldsymbol{\omega}\|^2 + 4\pi^2\eta\|\mathbf{n}\|^2$$

$$\geq \|\boldsymbol{\omega}\|^2 + 4\pi^2\eta\|\mathbf{n}\|^2 \cdot \frac{\|\boldsymbol{\omega}\|^2}{2\pi^2(1-\eta)^2}$$

$$\geq \frac{1+\eta^2}{(1-\eta)^2}\|\boldsymbol{\omega}\|^2 \quad \text{whenever } \|\mathbf{n}\| \geq 1.$$

This means that, $\boldsymbol{\omega} \in [-\pi(1-\eta), \pi(1-\eta)]^2$

$$1 \geq |\hat{\beta}_\gamma^\perp(\boldsymbol{\omega})|^2 \geq \underbrace{\frac{1}{1 + \mathcal{O}\left(\left(\frac{(1-\eta)^2}{1+\eta^2}\right)^\gamma\right)}}_{\xrightarrow[\gamma\to\infty]{} 1} + \mathcal{O}(2/3)^\gamma.$$

Since this is true for all $\eta > 0$ we have that

$$|\hat{\beta}_\gamma^\perp(\boldsymbol{\omega})|^2 \xrightarrow[\gamma\to\infty]{} 1 \text{ for all } \boldsymbol{\omega} \in]-\pi,\pi[^2.$$

Thanks to the orthonormality relation $1 = \sum_{\mathbf{n}\in\mathbb{Z}^2} |\hat{\beta}_\gamma^\perp(\boldsymbol{\omega} + 2\mathbf{n}\pi)|^2$, we also find that $|\hat{\beta}_\gamma^\perp(\boldsymbol{\omega})|^2 \to 0$ in every square $\boldsymbol{\omega} \in 2\mathbf{n}\pi +]-\pi,\pi[^2$ with $\mathbf{n} \in \mathbb{Z} \setminus \{\mathbf{0}\}$. Finally, because of the inequality $\left|\hat{\beta}_\gamma([\boldsymbol{\omega}])\right|^2 \leq A_\gamma(e^{j\boldsymbol{\omega}})$ (see Lemma 1) we also have that $|\hat{\beta}_\gamma^\perp(\boldsymbol{\omega})|^2 \leq \|[\boldsymbol{\omega}]\|^{2\gamma}/\|\boldsymbol{\omega}\|^{2\gamma}$ which implies that $|\hat{\beta}_\gamma^\perp(\mathbf{n}\pi)|^2 \leq (2\pi^2)^\gamma/\|\mathbf{n}\pi\|^{2\gamma} \leq (2/3)^\gamma$ when $\|\mathbf{n}\|^2 \geq 3$. Since this expression tends to 0 as $\gamma \to \infty$, we can now conclude that $|\hat{\beta}_\gamma^\perp(\boldsymbol{\omega})|^2$ tends to zero when $\boldsymbol{\omega} \in \mathbb{R}^2 \setminus [-\pi,\pi]^2$, which proves the convergence of $\hat{\beta}_\gamma^\perp(\boldsymbol{\omega})$ to $\mathrm{rect}(\frac{\omega_1}{2\pi}) \cdot \mathrm{rect}(\frac{\omega_2}{2\pi})$. Figure 11 illustrates the convergence. ∎

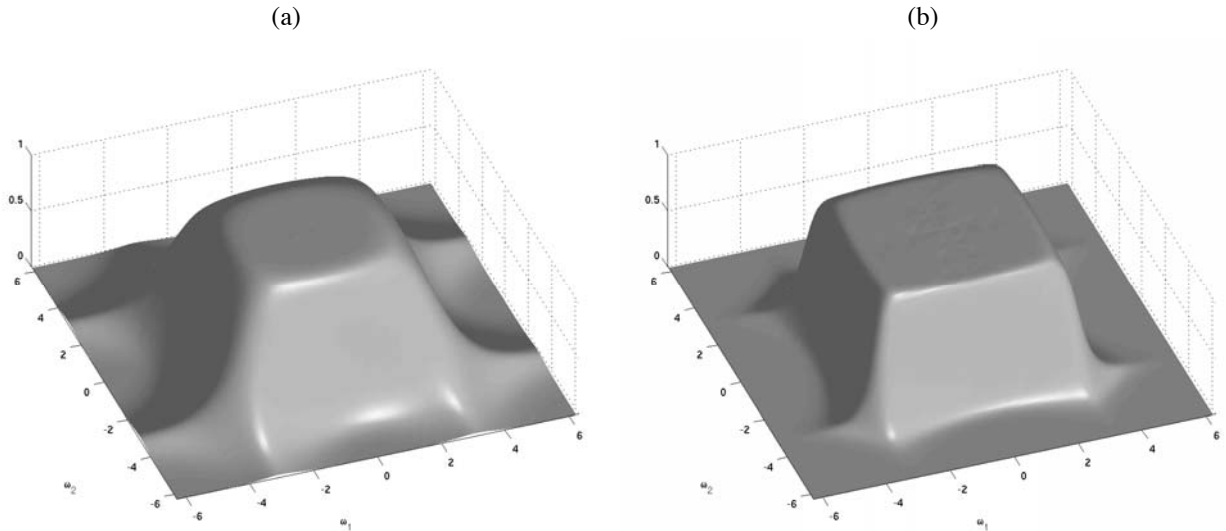(a)   (b)

Fig. 11. Frequency responses $\left|\hat{\beta}_{\gamma}^{\perp}\right|$ for (a) $\gamma = 4$, (b) $\gamma = 10$.

REFERENCES

[1] S. Mallat, "A theory for multiresolution signal decomposition: The wavelet decomposition," *IEEE Trans. Pattern Anal. Mach. Intell.*, vol. 11, pp. 674–693, 1989.

[2] I. Daubechies, *Ten Lectures on Wavelets*, PA: SIAM, Philadelphia, 1992.

[3] M. Unser and T. Blu, "Wavelet theory demystified," *IEEE Transactions on Signal Processing*, vol. 51, no. 2, pp. 470–483, Feb. 2003.

[4] E. J. Candès and D. L. Donoho, *Curve and Surface Fitting*, chapter Curvelets—A surprisingly effective non-adaptive representation for objects with edges, Vanderbilt University Press, Saint-Malo, 1999.

[5] E. J. Candès and D. L. Donoho, "Ridgelets: a key to higher-dimensional intermittency?," *Phil. Trans. R. Soc. Lond. A.*, pp. 2495–2509, 1999.

[6] J. L. Starck, E. J. Candès, and D. L. Donoho, "The curvelet transform for image denoising," *IEEE Transactions on Image Processing*, vol. 11, no. 6, pp. 670–684, June 2002.

[7] V. Velisavljevic, P. L. Dragotti, and M. Vetterli, "Directional wavelet transforms and frames," in *Proceedings of the International Conference on Image Processing*. IEEE, June 2002, vol. 3, pp. 589–592.

[8] P. Vandergheynst and J.-F. Gobbers, "Directional dyadic wavelet transforms: design and algorithms," *IEEE Transactions on Image Processing*, vol. 11, no. 4, pp. 363–372, Apr. 2002.

[9] M. N. Do and M. Vetterli, "The finite ridgelet transform for image representation," *IEEE Transactions on Image Processing*, vol. 12, no. 1, pp. 16–28, Jan. 2003.

[10] M. N. Do and M. Vetterli, *Beyond Wavelets*, chapter Contourlets, Academic Press, 2003.

[11] V. Velisavljevic, B. Beferull-Lozano, M. Vetterli, and P. L. Dragotti, "Discrete multi-directional wavelet bases," in *Proceedings of the International Conference on Image Processing*. IEEE, Sept. 2003, vol. 1, pp. 1025–1028.

[12] M. Unser and T. Blu, "Fractional wavelets, derivatives, and Besov spaces," in *Proceedings of the SPIE Conference on Mathematical Imaging: Wavelet Applications in Signal and Image Processing X*, San Diego, CA, Aug. 2003, SPIE, p. in press.

[13] Thierry Blu and Michael Unser, "On the fractional approximation order and Sobolev regularity of scaling functions," *SIAM J. Math. Anal.*, submitted.

[14] E. P. Simoncelli and E. H. Adelson, "Non-separable extensions of quadrature mirror filters to multiple dimensions," *Proceedings of the IEEE*, vol. 78, pp. 652–664, Apr. 1990.

[15] G. Karlsson and M. Vetterli, "Theory of two-dimensional multirate filter banks," *IEEE Transactions on Acoustics, Speech, Signal Processing*, vol. 38, no. 6, pp. 925–937, June 1990.

[16] E. Viscito and J. P. Allebach, "The analysis and design of multidimensional fir perfect reconstruction filter banks for arbitrary sampling lattices," *IEEE Transactions on Circuits and Systems*, vol. 38, no. 1, pp. 29–42, Jan. 1991.

[17] J. Kovačević and M. Vetterli, "Nonseparable multidimensional perfect reconstruction filter banks and wavelet bases for $\mathbb{R}^n$," *IEEE Transactions on Information Theory*, vol. 38, no. 2, pp. 533–555, Mar. 1992.

[18] J. Kovačević and M. Vetterli, "Nonseparable two- and three-dimensional wavelets," *IEEE Transactions on Signal Processing*, vol. 43, no. 5, pp. 1269–1273, 1995.

[19] Bin Han and Rong-Qing Jia, "Quincunx fundamental refinable functions and quincunx biorthogonal wavelets," *Mathematics of Computation*, vol. 71, no. 237, pp. 165–196, 2002.

[20] J. H. McClellan, "The design of two-dimensional digital filters by transformations," in *Proc. 7th Annual Princeton Conf. Inf. Sciences and Systems*, Princeton, USA, 1973, pp. 247–251.

[21] D. E. Dudgeon and R. M. Mersereau, *Multidimensional Digital Signal Processing*, Englewood Cliffs (Prentice-Hall), NJ, 1984.

[22] Manuela Feilner, Dimitri Van De Ville, and Michael Unser, "An orthogonal family of quincunx wavelets with continuously-adjustable order," *IEEE Transactions on Image Processing*, submitted for publication.

[23] T. Blu and M. Unser, "Wavelets, fractals, and radial basis functions," *IEEE Transactions on Signal Processing*, vol. 50, no. 3, pp. 543–553, Mar. 2002.

[24] I. J. Schoenberg, *Cardinal Spline Interpolation*, vol. 12, SIAM, Philadelphia, 1973.

[25] Robert L. Harder and Robert N. Demarais, "Interpolation using surface splines," *J. Aircraft*, vol. 9, pp. 189–191, 1972.

[26] Jean Duchon, "Interpolation des fonctions de deux variables suivant le principe de la flexion des plaques minces," *RAIRO Analyse Numérique*, vol. 10, no. 12, pp. 5–12, 1976.

[27] Jean Duchon, *Constructive theory of functions of several variables*, chapter Splines minimizing rotation-invariant semi-norms in Sobolev spaces, pp. 85–100, Springer, Berlin, 1977.

[28] R. Franke, "A critical comparison of some methods for interpolation of scattered data," *Math. Comp.*, vol. 38, pp. 181–200, 1982.

[29] Nira Dyn and David Levin, "Iterative solution of systems originating from integral equations and surface interpolation," *Numerical Analysis*, vol. 20, no. 2, pp. 377–390, 1983.

[30] M. D. Buhmann, "Radial basis functions," *Acta Numerica*, pp. 1–38, 2000.

[31] M. Fenn and G. Steidl, "Fast NFFT based summation of radial functions," *Sampling Theory in Signal and Image Processing*, vol. 3, no. 1, pp. 1–28, Jan. 2004.

[32] W. R. Madych and S. A. Nelson, "Polyharmonic cardinal spline," *Journal of Approximation Theory*, vol. 60, pp. 141–156, 1990.

[33] W. R. Madych and S. A. Nelson, "Polyharmonic cardinal splines: A minimization property," *Journal of Approximation Theory*, vol. 63, pp. 303–320, 1990.

[34] Ognyan Kounchev, *Multivariate polysplines: Applications to Numerical and Wavelet Analysis*, Academic Press, 2001.

[35] Christophe Rabut, "Elementary m-harmonic cardinal B-splines," *Numerical Algorithms*, vol. 2, pp. 39–62, 1992.

[36] Christophe Rabut, "High level m-harmonic cardinal B-splines," *Numerical Algorithms*, vol. 2, pp. 63–84, 1992.

[37] M. L. Glasser and I. J. Zucker, *Theoretical Chemistry: Advances and Perspectives*, vol. 5, chapter Lattice Sums in Theoretical Chemistry, pp. 69–139, Academic Press, 1980.

[38] Daniel Shanks, "Calculation and applications of Epstein Zeta functions," *Mathematics of Computation*, vol. 29, no. 129, pp. 271–287, Jan. 1975.

[39] E. Elizalde, "Zeta functions: formulas and applications," *Journal of Computational and Applied Mathematics*, vol. 118, pp. 125–142, 2000.

[40] C. de Boor, R. Devore, and A. Ron, "Approximation from shift invariant subspaces of $L^2(\mathbb{R}^d)$," *Trans. Amer. Math. Soc.*, , no. 341, pp. 787–806, 1994.

[41] T. Blu and M. Unser, "Approximation error for quasi-interpolators and (multi-)wavelet expansions," *Applied and Computational Harmonic Analysis*, vol. 6, no. 2, pp. 219–251, Mar. 1999.

[42] W. R. Madych, "Polyharmonic splines, multiscale analysis, and entire functions," *International Series of Numerical Mathematics*, vol. 94, pp. 205–216, 1990.

[43] W. R. Madych, *Wavelets: A tutorial in theory and applications*, chapter Some elementary properties of multiresolution analyses of $L_2(\mathbb{R}^n)$, pp. 259–294, Academic Press, Boston, 1992.

[44] Charles Micchelli, Christophe Rabut, and Florencia I. Utreras, "Using the refinement equation for the construction of pre-wavelets iii: elliptic splines," *Numerical Algorithms 1*, , no. 4, pp. 331–352, 1991.

[45] A. Cohen and I. Daubechies, "Non-separable bidimensional wavelet bases," *Revista Matematica Iberoamericana*, vol. 9, pp. 51–137, 1993.

[46] M. Vetterli, "Multi-dimensional sub-band coding: Some theory and algorithms," *Signal Processing*, vol. 6, no. 2, pp. 97–112, Feb. 1984.

[47] J.-C. Feauveau, *Analyse multirésolution par ondelettes non orthogonales et bancs de filtres numériques*, Ph.D. thesis, Univ. Paris Sud, 1990.

[48] F. Nicolier, O. Laligant, and F. Truchetet, "B-spline quincunx wavelet transform and implementation in Fourier domain," in *Proc. SPIE*, Boston, Massachussets, USA, november 1998, vol. 3522, pp. 223–234.

[49] F. Nicolier, O. Laligant, and F. Truchetet, "Discrete wavelet transform implementation in Fourier domain for multidimensional signal," *Journal of Electronic Imaging*, vol. 11, no. 3, pp. 338–346, July 2002.

[50] M. Unser, A. Aldroubi, and M. Eden, "A family of polynomial spline wavelet transforms," *Signal Processing*, vol. 30, pp. 141–162, 1993.

[51] D. Gabor, "Theory of communication," *Journal of the IEE*, vol. 93, no. III, pp. 429–457, Nov. 1946.

[52] M. J. Bastiaans, "Gabor's expansion of a signal into Gaussian elementary signals," *Proceedings of the IEEE*, vol. 68, pp. 538–539, Apr. 1980.

[53] M. Porat and Y. Y. Zeevi, "The generalized Gabor scheme of image representation in biological and machine vision," *IEEE Transactions on Pattern Analysis and Machine Intelligence*, vol. 10, no. 4, pp. 452–468, 1988.

[54] I. Daubechies, "The wavelet transform, time-frequency localization and signal analysis," *IEEE Transactions on Information Theory*, vol. 36, no. 5, pp. 961–1005, 1990.

[55] J. Wexler and S. Raz, "Discrete gabor expansion," *Signal Processing*, vol. 21, pp. 207–220, 1990.

[56] T. S. Lee, "Image representation using 2D Gabor wavelets," *IEEE Transactions on Pattern Analysis and Machine Intelligence*, vol. 18, no. 10, pp. 959–971, 1996.

[57] H. G. Feichtinger and T. Strohmer, Eds., *Advances in Gabor Analysis*, Applied and Numerical Harmonic Analysis. Birkhäuser, 2002.

[58] J. F. Canny, "A computational approach to edge detection," *IEEE Transactions on Pattern Analysis and Machine Intelligence*, vol. 8, no. 6, pp. 679–698, 1986.

[59] M. Basu, "Gaussian-based edge-detection methods-a survey," *IEEE Transactions on Systems, Man and Cybernetics, Part C*, vol. 32, no. 3, pp. 252–260, Aug. 2002.

[60] M. Turner, "Texture discrimination by Gabor functions," *Biol. Cybern.*, vol. 55, pp. 71–82, 1986.

[61] J. G. Daugman, "Uncertainty relation for resolution in space, spatial frequency, and orientation optimized by two-dimensional visual cortical filters," *Journal of Optical Society of America A*, vol. 2, no. 7, pp. 1160–1169, 1985.

[62] David J. Field, "Relations between the statistics of natural images and the response properties of cortical cells," *Journal of Optical Society of America A*, vol. 4, no. 12, pp. 2379–2394, 1987.

[63] Brian A. Wandell, *Foundations of Vision*, Sinauer Associates, 1995.

[64] Dimitri Van De Ville, Thierry Blu, and Michael Unser, "Wavelets versus resels in the context of fMRI: establishing the link with SPM," in *SPIE's Symposium on Optical Science and Technology: Wavelets X*, San Diego CA, USA, Aug. 2003, SPIE, vol. 5207, pp. 417–425.

[65] Park. H. J. and H. S. Yang, "Invariant object detection based on evidence accumulation and Gabor features," *Pattern Recognition Letters*, vol. 22, pp. 869–882, 2001.

[66] V. Krüger and G. Sommer, "Gabor wavelet networks for efficient head pose estimation," *Image Vision Comput.*, vol. 20, no. 9–10, pp. 665–672, 2002.

[67] Ville Kyrki, Joni-Kristian Kamarainen, and Heikki Kälviäinen, "Simple Gabor feature space for invariant object recognition," *Pattern Recognition Letters*, vol. 25, pp. 311–318, 2004.

[68] T. Kanade and F. Kagalwala, "Reconstructing specimens using DIC microscope images," *IEEE Transactions on Systems, Man, and Cybernetics, Part B: Cybernetics*, vol. 33, no. 5, pp. 728–737, Oct. 2003.

[69] B. Bacchelli, M. Bozzini, and C. Rabut, *Curve and Surface Fitting*, chapter A fast wavelet algorithm for multi-dimensional signal using polyharmonic splines, pp. 21–30, NashboroPress, 2003.

[70] Thierry Blu, Dimitri Van De Ville, and Michael Unser, "Numerical methods for the computation of wavelet correlation sequences," *SIAM Journal on Numerical Analysis*, submitted.

[71] Mathworks Inc., "Wavelet toolbox 2.2," 2000.

[72] M. Frigo and S. G. Johnson, "FFTW: An adaptive software architecture for the FFT," in *Proceedings of ICASSP*, 1998, vol. 3, pp. 1381–1384.

[73] Milton Abramowitz and Irene A. Stegun, Eds., *Handbook of Mathematical Functions with Formulas, Graphs, and Mathematical Table*, Government Printing Office, 10 edition, 1972.